



18 **Abstract**

19           As seismic data collection continues to grow, advanced automated processing techniques  
20 for robust phase identification and event detection are becoming increasingly important.  
21 However, the performance, benefits, and limitations of different automated detection approaches  
22 have not been fully evaluated. Our study examines how the performance of conventional  
23 techniques, including the Short-Term Average/Long-Term Average (STA/LTA) method and  
24 cross-correlation approaches, compares to that of various deep learning models. We also evaluate  
25 the added benefits that transfer learning may provide to machine learning applications. Each  
26 detection approach has been applied to three years of seismic data recorded by stations in East  
27 Antarctica. Our results emphasize that the most appropriate detection approach depends on the  
28 data attributes and the study objectives. STA/LTA is well-suited for applications that require  
29 rapid results even if there is a greater likelihood for false positive detections, and correlation-  
30 based techniques work well for identifying events with a high degree of waveform similarity.  
31 Deep learning models offer the most adaptability if dealing with a range of seismic sources and  
32 noise, and their performance can be enhanced with transfer learning, if the detection parameters  
33 are fine-tuned to ensure the accuracy and reliability of the generated catalog. Our results in East  
34 Antarctic provide new insight into polar seismicity, highlighting both cryospheric and tectonic  
35 events, and demonstrate how automated event detection approaches can be optimized to  
36 investigate seismic activity in challenging environments.

37

38

39

40 **Plain Language Summary**

41 Given the large quantity of seismic data recorded for geologic investigations, the manual  
42 identification of earthquake arrivals is becoming less feasible, and automated detection  
43 approaches are becoming increasingly important. However, the benefits and limitations of  
44 different detection techniques have not been fully evaluated. We examine a range of automated  
45 detection approaches, applied to data recorded by seismic stations in Antarctica, to assess the  
46 performance of each method. Additionally, an approach called transfer learning is examined to  
47 determine if it can improve the accuracy and reliability of the automated detections. Our results  
48 highlight new seismic events in Antarctica, providing insights into both geologic processes and  
49 ice-sheet behavior.

50

51

## 52 **1. Introduction**

53           The accurate creation of earthquake catalogs for seismotectonic interpretation requires  
54 robust seismic phase identification, event association, and event detection; however, with the  
55 ever-increasing availability of seismic data, manual processing by human analysts is becoming  
56 less feasible. As such, automated processing techniques are becoming increasingly important.  
57 Some event detection techniques, such as the Short-Term Average/Long-Term Average  
58 (STA/LTA) method (Allen, 1978; Earle & Shearer, 1994), use relatively simple algorithms and  
59 provide rapid results without the need for extensive data pre-processing. Waveform based cross-  
60 correlation approaches, such as the matched filter (MF) technique (Gibbons & Ringdal, 2006;  
61 Peng & Zhao, 2009; Shelly et al., 2007), can also be applied to STA/LTA generated earthquake  
62 catalogs to identify new, closely located events with similar focal mechanisms to those in the  
63 initial catalog. However, STA/LTA may not perform well for low signal-to-noise ratio (SNR)  
64 data, and cross-correlation based approaches can sometimes generate spatially biased event  
65 catalogs (Herrmann & Marzocchi, 2021; Schaff & Beroza, 2004; Yoon et al., 2015). The  
66 shortcomings of these methods can also sometimes result in impulsive transient signals or distant  
67 regional/teleseismic signals being erroneously identified as local earthquakes (*e.g.*, Meng et al.,  
68 2012). In some cases, these challenges can be overcome using phase association algorithms,  
69 which analyze triggers from multiple stations to determine whether any combination displays  
70 arrival time sequences that align with characteristic seismic event patterns (Myers et al., 2007).

71           In recent years, advancements in machine learning techniques, coupled with the  
72 democratization of open-source software, have provided more sophisticated methods to  
73 automatically detect seismic events. In particular, convolutional neural networks (CNN), which  
74 perform a sequence of convolution, resampling, and non-linear transformations on raw  
75 waveform data, have shown promising results (Perol et al., 2018; Ross et al., 2018; Wu et al.,

76 2018; Zhou et al., 2019; Zhu et al., 2019) when compared to more traditional techniques (Earle  
77 & Shearer, 1994; Gibbons & Ringdal, 2006; Peng & Zhao, 2009; Shelly et al., 2007). CNN  
78 pickers are designed to provide the added advantage of identifying body wave phases on three-  
79 component seismograms, thereby simplifying earthquake association and relocation. However,  
80 machine learning algorithms are complex, computationally demanding, and typically require  
81 optimization to avoid false-positive event detections.

82 To date, only a few studies have evaluated the performance of different automated  
83 detection approaches with respect to one another or have attempted to combine detection  
84 techniques to achieve the best possible outcome (Münchmeyer et al., 2022; Neves et al., 2024; Si  
85 et al., 2024; Woollam et al., 2022; Yuan et al., 2023). Further, most of these previous studies  
86 have typically only examined select model pairs based on one or a few training datasets (*e.g.*,  
87 Han et al., 2023; Jiang et al., 2021; Perol et al., 2018; Vaezi & Van der Baan, 2015), and they  
88 largely focus on small magnitude, tectonic-related seismic events. Here, we compare the benefits  
89 and limitations of the STA/LTA technique (Earle & Shearer, 1994), the cross-correlation-based  
90 MF approach (Peng & Zhao, 2009), and a suite of deep learning models, including  
91 EQTransformer (EQT, Mousavi et al., 2020), PhaseNet (Zhu & Beroza, 2019), BasicPhaseAE  
92 (Woollam et al., 2019), and the Generalized Phase Detection (GPD) model (Ross et al., 2018).  
93 We also update the deep learning models with additional training data derived from this project,  
94 a process known as transfer learning. Despite the potential for transfer learning to enhance model  
95 adaptability and efficiency (Chai et al., 2020; Lapins et al., 2021), particularly in data-scarce  
96 environments, its adoption in seismic studies has not been as rapid or as extensive as in other  
97 domains of deep learning research. This gap presents an opportunity to investigate the full  
98 capabilities of transfer learning in automatic event detection. We test the performance of the

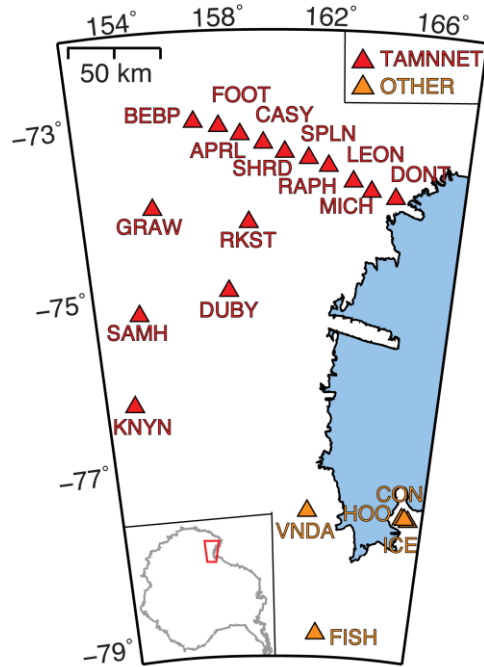
99 updated versus original deep-learning models using a range of metrics that evaluate each of their  
100 abilities to accurately determine the onset time of phase arrivals, to reliably classify phases as P-  
101 or S-waves, and to identify events while minimizing the number of false positives. These  
102 techniques are applied to a unique set of waveforms that contain a mixture of tectonic earthquake  
103 signals and seismic events generated by glacial movement (*e.g.*, icequakes). Collectively, our  
104 evaluation allows us to assess the efficacy of each algorithm when applied to a complex dataset.

105

## 106 **2. Data and Methods**

107       Broadband seismic deployments across the Antarctic continent have dramatically  
108 increased over the past several decades (*e.g.*, Anandkrishnan et al., 2000; Anthony et al., 2015;  
109 Hansen et al., 2015; Heeszel et al., 2013; Pyle et al., 2010), providing a valuable and challenging  
110 test dataset for automatic event detection. Seismic events in Antarctica are not only associated  
111 with tectonic sources (*e.g.*, Lough et al., 2013, 2018; Rowe et al., 2000) but are also caused by  
112 other natural phenomena, such as iceberg calving signals (*e.g.*, Chen et al., 2011; Riel et al.,  
113 2021; Winberry et al., 2020; Zoet et al., 2012) or ice-stream slip (*e.g.*, Guerin et al., 2021;  
114 Hudson et al., 2023; Nettles & Ekström, 2010; Winberry et al., 2014; Walter et al., 2011, 2015),  
115 which are collectively classified as icequakes. Our study focuses on a subset of seismic data  
116 recorded by 19 stations deployed in the Victoria Land region of East Antarctica (Fig. 1), which  
117 provide continuous seismic recordings for several years. Most of these stations (15) were part of  
118 the Transantarctic Mountains Northern Network (TAMNNET), which operated between 2012-  
119 2015 (Hansen, 2012; Hansen et al., 2015); however, we also incorporated data from two  
120 additional networks (ER, GT; Fig. 1; ASL/USGS, 1993). This dataset allows us to provide  
121 unique constraints on polar seismic activity and to evaluate automated event detection  
122 performance in a region with limited station coverage.

123



124

125

126 **Figure 1.** Map highlighting the examined seismic stations in Victoria Land, East Antarctica. Red  
 127 triangles denote TAMNNET stations (Hansen et al., 2015), and orange triangles denote stations  
 128 from other networks. Station names are also provided. The location of the main map in relation  
 129 to the rest of Antarctica is highlighted in the inset on the lower left.

130

131

132

133

134

135

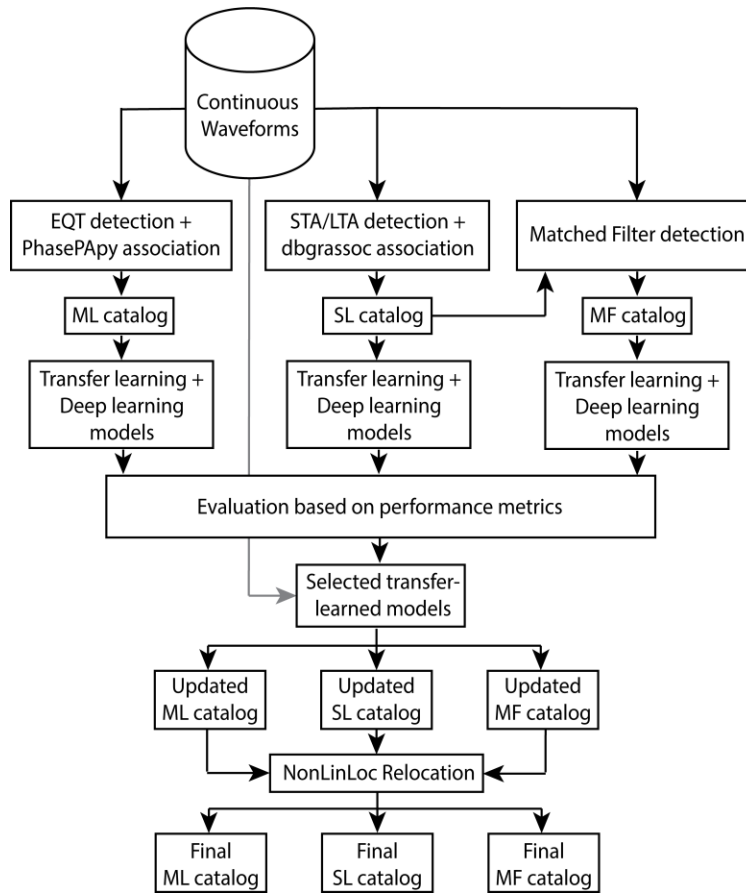
136

137

138

139

We developed a comprehensive workflow to assess the performance of different  
 automated event detection techniques (Fig. 2). The continuous waveforms recorded by the East  
 Antarctic stations (Fig. 1) were used to develop three starting catalogs, based on the STA/LTA,  
 MF, and EQT machine learning approaches, respectively. Each catalog was then used to fine-  
 tune a series of deep learning models via transfer learning, and their performance was evaluated  
 with various metrics. The fine-tuned detection approach that worked best for our Antarctic  
 dataset was then applied to update the three catalogs, and the events were relocated using a  
 uniform velocity model. Each analysis step is described in detail in the following sections.



140

141

142 **Figure 2.** Flowchart summarizing the different automated seismic detection techniques  
 143 examined in our study and the associated analysis steps.

144

145 **3. Automated Detection Approaches**

146

147

148

149

150

151

152

153

As shown in Figure 2, three different automated event detection approaches were initially evaluated by our study, including the STA/LTA method, the MF technique, and a machine learning-based approach using the EQT algorithm. The following subsections highlight the contributions and limitations of each approach as they are applied to our East Antarctic dataset (Fig. 1).

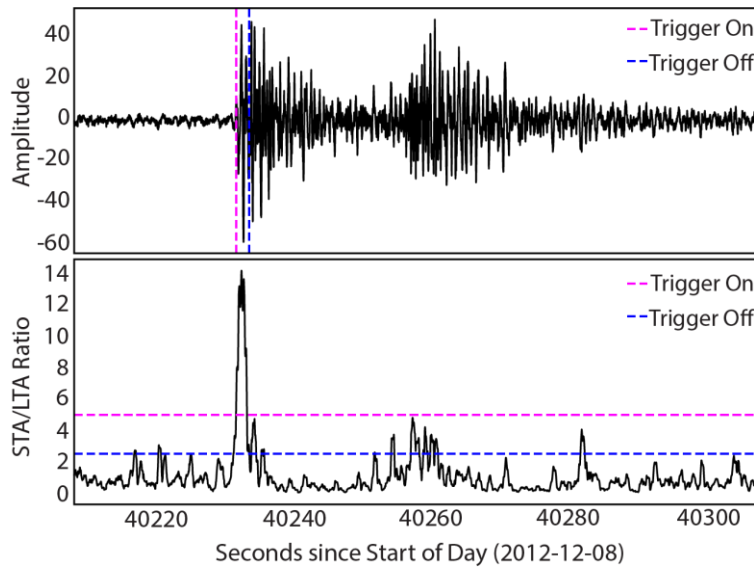
*3.1. STA/LTA Method (SL Catalog)*

The STA/LTA method (Allen, 1978; Earle & Shearer, 1994) detects high-frequency events in continuous data by identifying signals that have a mean energy ratio above some

154 specified threshold. The STA window contains the dominant frequency of the events the  
155 algorithm aims to detect, while the LTA window contains mostly background noise, which  
156 should exceed the period of the lowest frequency seismic signal of interest (Trnkoczy, 2009). In  
157 continuous data, a trigger is declared when the STA/LTA ratio at any sample point surpasses a  
158 pre-defined threshold, indicating that an event is possibly occurring (Allen, 1978; Baer &  
159 Kradolfer, 1987). The algorithm remains in this triggered state until the ratio decreases below a  
160 specified trigger-release threshold (Fig. 3). One of the strengths of the STA/LTA method is that  
161 it does not require any prior knowledge about an event's waveform nor its source (Yoon et al.,  
162 2015); however, it does have limitations. For instance, S-waves may not be accurately detected if  
163 they arrive within the P-wave coda, and this can be problematic because S-waves are important  
164 when trying to determine the depth and origin time for an earthquake. The STA/LTA method is  
165 also highly sensitive to the level of noise in the data, and it may not perform well with dense  
166 earthquake sequences and/or emergent arrivals (Schaff & Beroza, 2004).

167 For our study, we designated short-term and long-term window lengths of 0.5 and 8.0 s,  
168 respectively. We also set the SNR trigger and trigger-release thresholds to 5 and 2.5, respectively  
169 (Fig. 3). Detections were associated with the Antelope dbgrassoc association module (BRTT,  
170 2011), using a pre-computed travel-time grid based on the IASP91 reference velocity model  
171 (Kennett & Engdahl, 1991), and events were declared if they were recorded by at least four  
172 stations. Between 2012-2014, 560 events were detected using the STA/LTA approach and  
173 automatic association, thereby forming our SL catalog (Fig. 2). The data were then bandpass  
174 filtered between 2-5 Hz to highlight the signals of interest, and all phase arrivals were manually  
175 reviewed and adjusted, as needed. These additional processing steps allowed us to refine our SL  
176 catalog of high-quality events with well-determined phase arrivals.

177



178

179

180 **Figure 3.** Example illustrating STA/LTA detection thresholds. The upper panel shows an event  
 181 waveform that was detected by the STA/LTA approach, and the lower panel shows the  
 182 STA/LTA ratio for the triggered event. Pink lines denote the trigger threshold (5) and trigger  
 183 time; blue lines denote the trigger release threshold (2.5) and corresponding time.

184

### 185 3.2. Matched Filter Approach (MF Catalog)

186

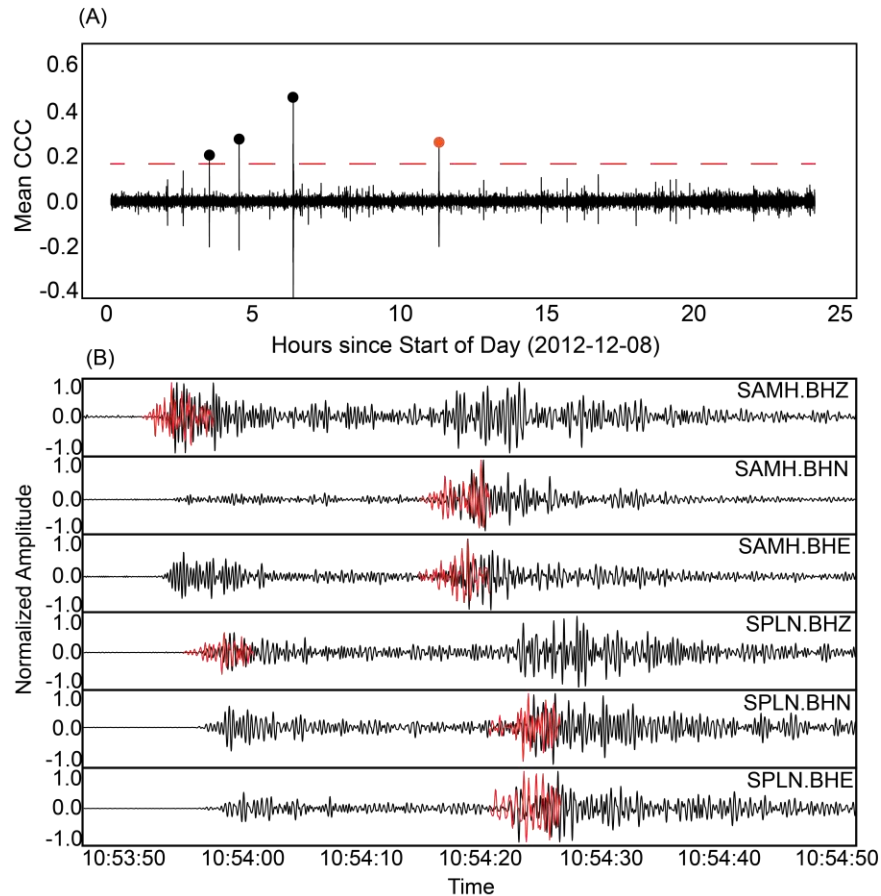
187 The MF technique, also known as template matching or network-based waveform cross-  
 188 correlation (Gibbons & Ringdal, 2006; Peng & Zhao, 2009; Shelly et al., 2007), provides another  
 189 approach to automatically detect seismic arrivals, which is based on waveform similarity. Pre-  
 190 defined template waveforms are cross-correlated with continuous data over successive windows,  
 191 and signals exceeding a specified correlation threshold are identified as detections (Fig. 4).

191

192 Generally, the MF approach performs better than the STA/LTA method (Sect. 3.1) when dealing  
 193 with low SNR data. However, since the template events are often manually determined, the MF  
 194 method can be time consuming during its initial stages when building the template catalog (if  
 195 one does not already exist from a regional seismic network or other source). Furthermore, since  
 the approach relies on waveform similarity, seismic signals that differ significantly from the

196 template events may go undetected, leading to an incomplete catalog (Cianetti et al., 2021; Li et  
 197 al., 2018; Yoon et al., 2015).

198



199

200 **Figure 4.** (A) Mean cross-correlation coefficients (CCC) determined by matching a template  
 201 event, which occurred at 06:13:14 on 2012-12-08, against a full day (2012-12-08) of continuous  
 202 data. Dots denote detections whose CCC values exceed the detection threshold, which is twelve  
 203 times the MAD (red dashed line). The orange dot marks the detected event shown in panel (B).  
 204 (B) Examples illustrating waveform cross-correlation. Template waveforms (red) are plotted on  
 205 top of the continuous data (black), highlighting detected events from the MF approach. Station  
 206 names and components are indicated on the right. Amplitudes have been normalized so their  
 207 absolute maximum values are equal to one. This was done to better illustrate the waveform  
 208 comparisons.

209

210 Using EQcorrscan (Chamberlain et al., 2018), all identified events in the SL catalog were  
 211 treated as template events (Fig. 2), which were cross-correlated with the bandpass filtered (2-5  
 212 Hz) continuous data to identify additional seismic signals (Fig. 4). This bandpass was chosen

213 based on close examination of the template coda, the density of seismic stations in the region, as  
214 well as our prior experience working with Antarctic data, where higher frequency information  
215 can become scattered by the ice sheet (Bentley & Kohnen, 1976) and thus incoherent when  
216 attempting template matching. Each template event was defined by the portion of the waveform  
217 0.5 s before the event's P-wave arrival and 6 s after its S-wave arrival (Peng et al., 2014). The  
218 templates were shifted by 0.025 s (1 sample) increments through the continuous waveforms, and  
219 correlation coefficients were computed for each increment. Mean correlation coefficients were  
220 then determined by stacking the coefficient values across all stations and components (Fig. 4).  
221 The relative quality of each cross-correlated, matched waveform was evaluated using the median  
222 absolute deviation (MAD; Shelly et al., 2007), which is a measure of dispersion calculated as the  
223 median of the absolute difference between each data point for the mean correlation coefficient.  
224 The MAD value helps to estimate the variability in data distribution due to uncorrelated noise,  
225 thereby providing a robust measure to identify outliers. For a normally distributed dataset, the  
226 standard deviation is 1.4826 times the MAD (Hampel, 1974). Due to the noisy nature of real  
227 seismic data and the relatively long-period bandpass chosen for this project, a conservative  
228 threshold of 12 times the MAD was chosen, and signals that exceed this MAD value are  
229 identified as positive event detections (Fig. 4; *e.g.*, Skoumal et al., 2015; Yao et al., 2021).

230 A time domain, phase-pick SNR threshold was also applied to further ensure robust  
231 detections. For a given phase, the SNR was calculated by taking the maximum amplitude of the  
232 signal window and dividing it by the root-mean-square of the noise window. The noise windows  
233 start 6 s before the phase of interest, and both the signal and noise windows had lengths of 5.5 s  
234 (Fig. S1 in Supporting Information). The SNR threshold was subsequently determined by  
235 comparing the pick-specific SNR values obtained from all detected picks for each seismic event.

236 This additional processing step is not only important for robust event detections, but it also helps  
237 to remove unwanted signals, such as teleseismic events that originate from distant earthquakes.  
238 Sometimes teleseismic signals can be mistakenly detected in MF catalogs for local events, and  
239 this can adversely affect the accuracy of local event detections because teleseismic events have  
240 unique seismic waves and frequency contents (Waldhauser & Schaff, 2007). We determined that  
241 maintaining a SNR greater than 2.0 for both the P and S picks (Fig. S1 in Supporting  
242 Information) effectively helps to limit the influence of teleseismic events and reduces the number  
243 of false detections. With the MAD and SNR criteria applied, our MF catalog includes 4,577 local  
244 events (Fig. 2).

### 245 *3.3. Machine Learning Approach (ML Catalog)*

246 In addition to the STA/LTA and the MF techniques, we also utilized EQT, a machine  
247 learning-based signal detector and phase picker that was trained on a diverse seismic dataset  
248 (Mousavi et al., 2020). Further details about EQT and its architecture are provided in Section 4.1.  
249 We implemented the EQT picker within the easyQuake Python package (Walter et al., 2021) to  
250 identify P- and S-wave picks within the continuous data. The easyQuake associator, which is a  
251 modified version of PhasePApy (Chen & Holland, 2016), was used to aggregate pick  
252 information and declare event detections. Probability thresholds of 0.1, 0.1, and 0.3 were  
253 specified for the P-wave picks, S-wave picks, and event detections, respectively. In total, 1,728  
254 events were detected in the East Antarctic dataset, which compose our initial machine learning  
255 (ML) catalog (Fig. 2). It should be noted that this catalog is distinguished from those derived  
256 from transfer-learning in later sections because it was generated using phase picks that were  
257 based on the original model and parameters specified by Mousavi et al. (2020).

## 258 **4. Transfer Learning**

259 Each of the catalogs described in Sections 3.1-3.3 were used in a transfer learning process  
260 to adapt a series of pre-trained deep learning models. Instead of retraining an entire model from  
261 scratch with randomly initialized parameters or different model architecture, a strategy called  
262 fine-tuning is employed, where the original model and its architecture serve as the starting point,  
263 and training continues with newly added data, thereby refining the model (Pan & Yang, 2010).  
264 Transfer learning not only leads to better model performance, but it also overcomes some of the  
265 limitations of traditional models that assume training and testing datasets are independent and are  
266 identically distributed (Tan et al., 2018).

267 The effectiveness of transfer learning has been proven in various fields (Long et al.,  
268 2013, 2015; Pan et al., 2011), and while its adoption within the field of seismology has been  
269 relatively limited so far, the technique demonstrates promising potential. For instance, Zhu et al.  
270 (2019) used a CNN-based Phase-Identification Classifier (CPIC), which was initially trained on  
271 a dataset with 30,146 labeled phases from the aftershock sequences of the 2008  $M_w$  7.9  
272 Wenchuan earthquake, to develop a more complete aftershock catalog for the same area.  
273 Additionally, when fine-tuned on a smaller dataset from Oklahoma, the CPIC achieved 97%  
274 accuracy. This study highlights the potential for transfer learning applications to identify events  
275 in regions with no or few labeled phases. In a different study, Chai et al. (2020) enhanced the  
276 capabilities of the PhaseNet model (Zhu & Beroza, 2019), which was originally trained on data  
277 from regional seismic networks, to efficiently handle microseismic data from South Dakota.  
278 About 3,600 three-component seismograms and associated manual picks were used in the  
279 transfer learning process, and the performance of the retrained model exceeded that of the  
280 original PhaseNet model by over 10% in terms of precision and recall (see Sect. 4.3). Compared

281 to human expert detections, 32% fewer P-wave picks were made, but the fine-tuned model  
282 identified 48% more S-wave picks.

283 We implemented our transfer learning process with Seisbench, a toolbox for machine  
284 learning in seismology (Ho, 2024; Münchmeyer et al. 2022; Woollam et al., 2022). Various deep  
285 learning model architectures were utilized, including PhaseNet (Zhu & Beroza, 2019),  
286 BasicPhaseAE (Woollam et al., 2019), GPD (Ross et al., 2018), and EQT (Mousavi et al., 2020),  
287 which are more fully described in Section 4.1. These models were selected given their distinct  
288 yet interrelated approaches to seismic signal processing. Additionally, these models share a  
289 common approach in terms of pre-processing the seismic data. Regardless of their specific  
290 architectures or use cases, they all rely on uniformly sampled data, typically at 100 Hz. If the  
291 original data has a different sampling rate, it is resampled to ensure uniformity. The data  
292 windows used by these models vary in length, but they all incorporate multiple types of seismic  
293 signals, including P-waves, S-waves, and noise, within their respective networks.

#### 294 *4.1 Deep Learning Models*

295 The PhaseNet CNN (Zhu & Beroza, 2019) was developed as a U-Net architecture, which  
296 functions as an encoder-decoder mechanism that pulls significant features from input data and  
297 subsequently expands them to generate predictions of equivalent size outputs (Ronneberger et  
298 al., 2015). While the U-Net was initially created for a broad range of image processing  
299 applications, this approach has been adapted for earthquake phase detection. Three-component  
300 seismograms are sampled using 30 s windows that include both P- and S-wave arrivals, and these  
301 samples serve as the input for PhaseNet. The waveform data are then processed through an  
302 iterative down-sampling and up-sampling procedure. During down-sampling, the encoder  
303 reduces the dimensionality of the raw seismic data and extracts essential features associated with

304 the seismic phase arrivals. The condensed information provided by the encoder is then increased  
305 in dimensionality through up-sampling by the decoder, which converts the information into  
306 detailed probability distributions for P-waves, S-waves, and noise at each point in time  
307 (Goodfellow et al., 2016; Zhu & Beroza, 2019). For seismic applications, PhaseNet was  
308 originally trained and evaluated using 779,514 waveforms containing labeled P- and S-wave  
309 arrivals from local earthquakes recorded in northern California (Zhu & Beroza, 2019).

310 BasicPhaseAE, which is another U-Net-like CNN phase detector, employs three 6 s input  
311 windows, with each window sampling an individual component (Woollam et al., 2019). The  
312 structure of BasicPhaseAE is similar to PhaseNet, but it differs in a few aspects. BasicPhaseAE  
313 uses smaller filter sizes and omits convolutions without stride, which refers to the step size that  
314 the filter matrix moves across the input matrix during the convolution process. In addition,  
315 BasicPhaseAE lacks residual connections, which are essentially shortcuts or bypass routes that  
316 enable the gradient to be back-propagated directly to earlier layers (Woollam et al., 2019;  
317 Münchmeyer et al., 2022). The input data, which consists of labels or classes of seismic data  
318 (e.g., P-waves, S-waves, noise), undergo several transformations. Convolutional operations first  
319 extract the characteristic features for each class. During training, the model uses a designated 6 s  
320 window of data that is then divided into sequential sub-windows, each 0.4 s in length. The sub-  
321 windows are randomly shuffled to prevent the CNN from learning irrelevant temporal patterns.  
322 Extracted features then undergo multiple resampling stages, with a rectified linear unit activation  
323 function applied at each stage. The final architecture comprises three convolutional layers and  
324 three up-sampling layers. The network ultimately determines the probability of a P-wave, S-  
325 wave, or noise for every time sample in the input window. BasicPhaseAE was initially trained

326 and evaluated using 11,000 waveforms from earthquakes located within the Iquique region in  
327 northern Chile (Woollam et al., 2019).

328         The GPD model is a phase identification CNN with six layers, including four convolution  
329 layers and two fully connected layers (Ross et al., 2018). Rectified linear units serve as the  
330 activation function for each layer, and batch normalization is applied throughout. GPD operates  
331 on a short 4 s input window that advances five samples (0.05 s) after each prediction to create a  
332 new, slightly overlapped 4 s window for the next prediction (Münchmeyer et al., 2022). Each  
333 advanced window is then classified as a P-wave arrival, S-wave arrival, or noise. The GPD  
334 model was originally trained and evaluated using 4.5 million three-component seismic records,  
335 evenly distributed amongst P- and S-wave seismograms and noise (Ross et al., 2018). Using a  
336 multi-class cross-entropy loss for training, the GPD model has been shown to effectively detect  
337 and identify seismic phases in various datasets (Münchmeyer et al., 2022; Woollam et al., 2022).

338         EQT is a model designed for simultaneous seismic event detection, phase identification,  
339 and onset timing determination. This model was originally trained on a portion of the STEAD  
340 dataset (Mousavi et al., 2019), a global collection of 1.2 million hand-labeled earthquake and  
341 noise waveforms. EQT operates on 60 s windows of three-component seismic data. Its  
342 architecture comprises a deep encoder and three separate decoders, and it integrates convolution,  
343 long short-term memory (LSTM) units, residual connections, and attention mechanisms  
344 (Mousavi et al., 2020). The encoder processes the seismic data into high-level contextual  
345 representations, while the decoders convert these representations into probability sequences for  
346 events as well as for P- and S-wave detections. LSTM, which resembles human auditory memory  
347 processing, and attention mechanisms, which simulate selective focusing in high-resolution  
348 areas, work in tandem to enhance the model's performance (Gers et al., 1999). The attention

349 mechanisms function on two levels: global for earthquake events and local for phases within  
350 those events. During training, EQT employs data augmentation techniques, such as adding  
351 Gaussian noise, introducing gaps, and removing channels, which are implemented to enhance the  
352 model's robustness, teaching it how to handle various real-world data imperfections and  
353 irregularities. This helps to improve its overall performance and generalization ability (Mousavi  
354 et al., 2020).

355       Each of the above models has a different level of complexity, adaptability, and suitability  
356 for seismic datasets. For example, since BasicPhaseAE lacks residual connections, which are  
357 shortcuts that skip one or more layers to help train deep neural networks, its learning efficiency  
358 may be lower compared to PhaseNet (Münchmeyer et al., 2022). Compared to EQT, GPD is  
359 much slower, but it requires less memory. Further, the sophisticated EQT architecture and its  
360 comprehensive functionality may require more computational resources for complex analyses.  
361 We evaluate the performance of each model in relation to one another using our East Antarctic  
362 catalogs described in Sections 3.1-3.3, but it should be emphasized that the most suitable model  
363 for a given investigation depends on the type of data, the available processing time, and the  
364 computational resources available. We did not evaluate the relative computational performance  
365 of the specific algorithms in this study.

#### 366 *4.2 Applying Transfer Learning to the East Antarctic Catalogs*

367       Each of the pre-trained models described in the previous section were fine-tuned via  
368 transfer learning using each of the event catalogs (Sects. 3.1-3.3). The SL, MF, and ML catalogs  
369 contain a total of 1,536, 13,731, and 5,388 waveform segments, respectively. The metadata for  
370 each catalog were assembled into a QuakeML-formatted file, and we also developed HDF5-  
371 formatted files by combining the event metadata with the waveforms, similar to the STEAD

372 dataset format (Mousavi et al., 2019), for inclusion into Seisbench (Ho, 2024; Woollam et al.,  
373 2022). Each catalog was divided into a training subset, which is composed of 70% of the data, a  
374 validation subset, which contains 15% of the data, and a testing subset, which includes the  
375 remaining 15% of the data. The training subset was used to adjust the model’s weights and  
376 biases during the transfer learning process, while the validation subset was used to fine-tune the  
377 model’s hyperparameters. The validation subset was also essential in determining which model  
378 iteration performed the best, using the parameters described in Section 4.3. Once the optimal  
379 model configuration was identified based on the validation subset's results, the updated model  
380 was then evaluated on the testing subset. The final, reported results (Section 5) are based on this  
381 evaluation of the testing subset, thereby ensuring an unbiased assessment of each models’  
382 performance on unseen data.

383         Using the Münchmeyer et al. (2022) data augmentation techniques within SeisBench  
384 (Woollam et al., 2022), we built training pipelines, which are a series of steps that prepare and  
385 transform the waveform data for model training. Since our waveforms are long compared to each  
386 aforementioned model input length, a two-step approach was employed for window selection.  
387 First, for two-thirds of the training subset, windows were selected to ensure that they contained  
388 at least one labeled pick. For the remaining one-third, the windows were randomly selected from  
389 the entire waveform, and they may or may not include labeled picks. This approach guarantees  
390 that the training subsets are not overwhelmed by noise samples, which is particularly important  
391 for models with short input windows (*e.g.*, PhaseNet, BasicPhaseAE, GPD). The same approach  
392 was also applied to the validation subset.

393         Additionally, as part of the transfer learning process for each catalog, we employed the  
394 Adam optimizer (Kingma & Ba, 2014), which efficiently updates the model parameters to

395 minimize the error between predicted and actual values. A corresponding learning rate of 0.001  
396 was selected, which controls the magnitude of changes made to the model parameters during  
397 updates and ensures a steady convergence without overshooting (*i.e.*, where the model might  
398 skip over the optimal parameters). Further, a batch size of 256 was used in the optimizer, which  
399 means that 256 training samples were processed together during each iteration. This helps to  
400 balance computational efficiency and the quality of the model's gradient estimation (Coleman et  
401 al., 2017; Smith, 2018). Early stopping was also employed to obtain an optimal model. This  
402 strategy halts the training when the validation loss (a measure of prediction error) throughout the  
403 entire training subset fails to improve after ten successive cycles (epochs).

#### 404 *4.3. Evaluating Model Performance*

405 To evaluate each fine-tuned, deep learning model's ability to differentiate between  
406 seismic events and noise, we adopted the approach of Münchmeyer et al. (2022). First, a 30 s  
407 window of a random seismic waveform from either the validation or testing subset is analyzed to  
408 determine if it contains an event onset (*i.e.*, a first arriving seismic wave). Noise samples are also  
409 extracted from the window using labeled noise traces, if present. Otherwise, the noise sample is  
410 defined based on the presence or absence of P-wave and S-wave arrivals. That is, windows  
411 containing neither P- nor S-wave arrivals are labeled as noise, while those with either or both are  
412 labeled as an event. The event and noise labels were used as "ground truth" to compare with our  
413 models' predictions.

414 A variety of metrics are used to evaluate the performance of each model. First, to assess a  
415 model's ability to accurately identify event onsets while minimizing false positives, we  
416 examined the receiver operating characteristics (ROC), the area under the curve (AUC), and the  
417 F1 score. The ROC describes the true and false positive rates across all possible detection

418 thresholds, allowing for different trade-offs between these rates, depending on the application  
419 scenario (Fawcett, 2006). For example, in early earthquake warning systems, a high true positive  
420 rate is important to ensure timely alerts, even if it means getting some false alarms (Meier et al.,  
421 2020). Alternatively, in a tomography research setting, where detection precision might be  
422 prioritized, reducing false positives could be more important, even if it means potentially missing  
423 some weaker seismic events. The AUC is a single value that defines the area under the ROC  
424 curve. It quantifies the overall ability of the model to distinguish between positive and negative  
425 classes. An AUC of one indicates a perfect model, meaning the model can identify all events  
426 correctly without any false positives. Conversely, an AUC of 0.5 represents a random model  
427 (Hanley & McNeil, 1982). The F1 score is the harmonic mean of the precision (*i.e.*, the number  
428 of correct detections among all detections) and recall (*i.e.*, the number of detections among all  
429 possible detections). It serves as a combined measure of the model's sensitivity and specificity.  
430 As part of the transfer learning process, the AUC value is selected to optimize the F1 score,  
431 thereby fine-tuning the model to achieve an optimal trade-off between the false positive rate and  
432 the true positive rate.

433 In order to measure each model's binary classification performance, we used the  
434 Matthews Correlation Coefficient (MCC). It is ambiguous to assign P and S phases as positive  
435 and negative classes, and the MCC is insensitive to class assignment (Chicco & Jurman, 2020;  
436 Matthews, 1975; Münchmeyer et al., 2022). We analyzed 10 s windows containing exactly one  
437 phase arrival to determine if that arrival is a P- or an S-wave. The MCC is calculated as the  
438 correlation coefficient of the confusion matrix, and its value ranges from -1 (total disagreement)  
439 to 1 (full agreement). Even in cases of class imbalance, the MCC provides an appropriate  
440 measure for binary classification performance (Münchmeyer et al., 2022; Powers, 2011). Further,

441 the MCC value was selected to optimize the phase threshold, which is used to calibrate the P-  
442 and S-wave pick probability thresholds. The pick probability indicates the likelihood of a  
443 specific data point corresponding to a seismic phase arrival (*i.e.*, a P- or an S-wave signal), where  
444 a higher probability directly correlates with a heightened level of confidence from the model  
445 regarding the presence of an arrival at the identified data point. For the P pick threshold, we  
446 multiplied the detection threshold by the square root of the phase threshold. This adjustment  
447 enhances the P-wave detection sensitivity and improves identification of these arrivals. For the S  
448 pick threshold, we adopted a more conservative approach, dividing the detection threshold by the  
449 square root of the phase threshold. This approach was taken to minimize the risk of false  
450 positives.

451 Finally, we evaluated each model's ability to accurately determine the onset time of  
452 phase arrivals within a given catalog. Using the same 10 s window used for the MCC  
453 assessment, we calculated the pick residuals, which are the differences between the transfer-  
454 learning-based pick times and the labeled pick times from the validation subset. The residual  
455 distribution is analyzed using both the root-mean-square error (RMSE) and the mean absolute  
456 error (MAE). Lower values of RMSE and MAE indicate greater accuracy in predicting the phase  
457 arrival onset times. Together, these provide a comprehensive evaluation given their different  
458 performance, with RMSE being sensitive to outliers and MAE being less sensitive to them  
459 (Willmott & Matsuura, 2005).

460

## 461 **5. Results of Transfer Learning**

462 The performance metrics (Sect. 4.3) used to evaluate the four deep learning models (Sect.  
463 4.1) applied to each catalog (Sects. 3.1-3.3) elucidate the effects of transfer learning, and these

464 metrics are summarized in Tables 1-3. Generally, transfer learning has a positive effect on all  
465 models, as is evident from the AUC metrics, for example. The most dramatic change was  
466 observed for the ML catalog and the BasicPhaseAE model, where the AUC increased from 0.45  
467 to 0.81. That said, even models like GPD that already had a high AUC value (0.87) saw an  
468 increase (0.90). These results highlight the benefits of transfer learning. However, it is important  
469 to consider how each model defines an event detection. For instance, EQT needs both P- and S-  
470 wave labels to declare a detection within the seismogram time series (data from other stations is  
471 commonly aggregated during event association, discussed later), while GPD and PhaseNet do  
472 not. For scenarios where datasets might lack certain labels, such as in our SL and MF catalogs,  
473 this could lead to reduced performance, as reflected in the metric results. It is worth noting that  
474 our results are qualitatively comparable to those made by Münchmeyer et al. (2022) for the  
475 ETHZ dataset (Woollam et al., 2022), where some P- or S-wave labels were missing.

476         The RMSE and MAE metrics were reduced for both P and S picks across all catalogs,  
477 again indicating improved performance from the fine-tuning and transfer learning. Among all the  
478 models, EQT had the lowest of these metrics, indicating it had the highest pick accuracy.  
479 However, GPD also displayed significant improvements in RMSE and MAE and closely  
480 followed EQT across all catalogs (Tables 1-3). As for the MCC metrics, where higher values  
481 indicate better classification performance, every model exhibited a MCC rise following transfer  
482 learning. Comparing the three catalogs (Tables 1-3), the P and S picks are notably better  
483 classified in the ML catalog for all models, followed by the SL and then the MF catalog. These  
484 variations might be due to discrepancies in P- and S-wave labeling consistency across the  
485 catalogs. For example, the starting ML catalog was exclusively generated using EQT, perhaps  
486 leading to higher pick consistency and, as a result, lower RMSE and MAE values. As a result,

487 variations in performance across the three catalogs reveal that the efficiency of transfer learning  
488 also depends on the consistency and quality of the training subset.

489         Figure 5 shows an example of the pick probabilities for different deep learning models  
490 when applied to continuous data. EQT, GPD, and PhaseNet all have improved pick probabilities  
491 after transfer learning. The BasicPhaseAE pick probabilities did not increase post-transfer  
492 learning, and this could be due to the shorter input windows used by this model, together with its  
493 shorter filters and missing residual connections (Münchmeyer et al., 2022).

494

495 **Table 1.** Fine-tuned metric results before (left columns) and after (right columns) transfer  
 496 learning was applied to the ML catalog. AUC: Area under the Curve; RMSE: root-mean-square  
 497 error; MAE: mean absolute error; MCC: Matthews Correlation Coefficient.

Model	AUC		P picks RMSE		S picks RMSE		P picks MAE		S picks MAE		MCC	
PhaseNet	0.7	0.8	3.0	2.1	3.0	2.3	2.2	1.4	2.2	1.5	0.3	0.6
BasicPhaseAE	0.4	0.7	3.2	2.3	3.0	2.5	2.5	1.6	2.3	1.7	0.3	0.5
GPD	0.8	0.8	2.2	1.8	2.3	2.1	1.5	1.2	1.6	1.4	0.6	0.8
EQTransformer	0.7	0.7	3.4	1.8	3.0	1.8	2.4	1.1	2.1	1.1	0.6	0.9

498

499 **Table 2.** Fine-tuned metric results before (left columns) and after (right columns) transfer  
 500 learning was applied to the MF catalog. Columns are the same as in Table 1.

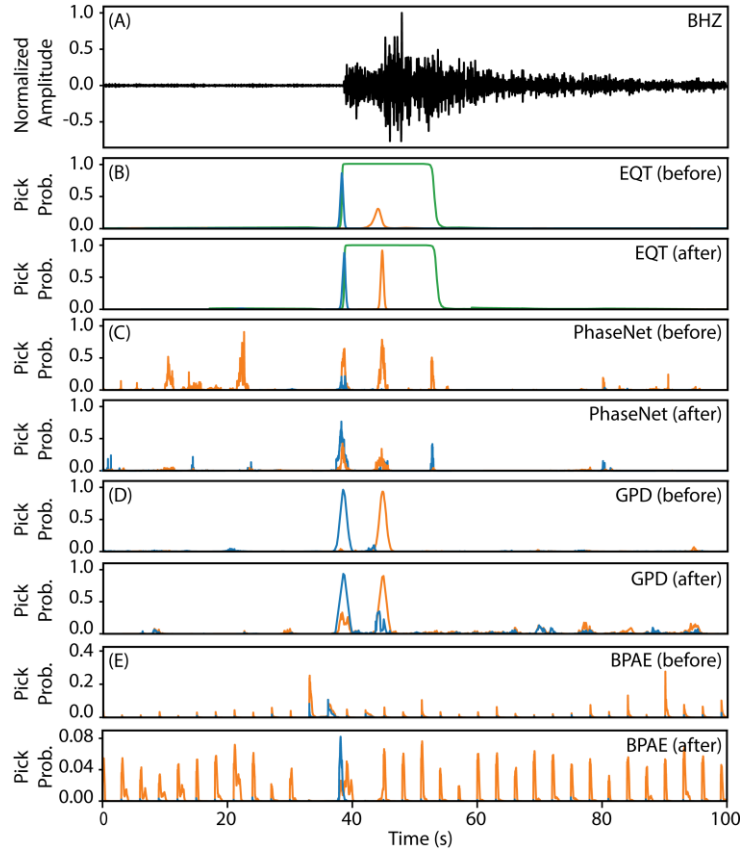
Model	AUC		P picks RMSE		S picks RMSE		P picks MAE		S picks MAE		MCC	
PhaseNet	0.7	0.9	2.8	1.1	2.4	1.2	1.8	0.5	1.6	0.6	0.3	0.7
BasicPhaseAE	0.4	0.8	3.2	1.1	2.8	1.3	2.5	0.6	2.0	0.7	0.3	0.7
GPD	0.8	0.9	1.2	0.6	1.3	0.8	0.6	0.3	0.7	0.4	0.7	0.9
EQTransformer	0.8	0.9	2.7	0.6	2.2	0.5	1.6	0.3	1.2	0.2	0.7	1.0

501

502 **Table 3.** Fine-tuned metric results before (left columns) and after (right columns) transfer  
 503 learning was applied to the SL catalog. Columns are the same as in Tables 1 and 2.

Model	AUC		P picks RMSE		S picks RMSE		P picks MAE		S picks MAE		MCC	
PhaseNet	0.7	0.8	2.0	1.4	2.4	2.0	1.2	0.8	1.6	1.2	0.4	0.8
BasicPhaseAE	0.4	0.7	2.8	1.7	2.7	2.2	2.0	1.0	1.9	1.4	0.4	0.7
GPD	0.8	0.9	1.4	0.9	2.0	2.0	0.8	0.6	1.3	1.2	0.8	0.9
EQTransformer	0.8	0.8	2.7	0.9	2.3	1.9	1.6	0.5	1.4	1.1	0.7	1.0

504



505

506

507 **Figure 5.** (A) Sample of the continuous Antarctic data recorded by station LEON (Fig. 1), and  
 508 corresponding pick probabilities for (B) EQT, (C) PhaseNet, (D) GPD, and (E) BasicPhaseAE  
 509 (BPAE). For each model, the top and bottom panels show the pick probabilities before and after  
 510 transfer learning, respectively (note that the vertical scales can vary by panel). Blue lines  
 511 correspond to P-waves, and orange lines correspond to S-waves. For EQT, the green lines show  
 512 the detection probability.

513

514

## 515 6. Model Assessment

### 516 6.1 Benefits and Limitations of Each Automated Event Detection Approach

517 Each automated event detection approach has its benefits and limitations, and the choice  
 518 of which approach to use depends on the objective of the study and the characteristics of the  
 519 dataset. The STA/LTA method stands out given its minimal pre-processing requirements,  
 520 straightforward algorithm, and low computational demands, making this technique efficient and

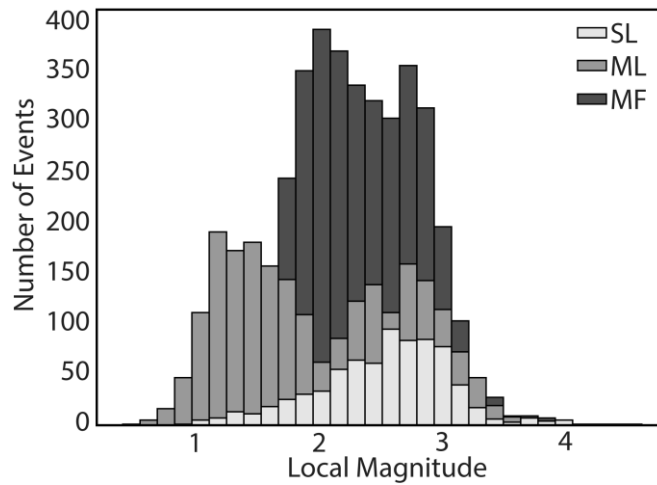
521 readily applicable. Notably, the approach can also identify low magnitude earthquakes if the data  
522 has sufficiently high quality (Fig. 6). However, as noted in Section 3.1, STA/LTA can struggle to  
523 identify emergent or low SNR arrivals (Schaff & Beroza, 2004; Yoon et al., 2015), which can  
524 make this technique more prone to errors, including an increased risks of false positive  
525 detections and/or detection failures (Kato et al., 2012). This limitation is partly due to the nature  
526 of the STA and LTA window lengths, which are not adjusted during the detection process  
527 (Trnkoczy, 2009) and hence restrict the method's ability to adapt to varying seismic signal  
528 characteristics. Figure S2 in the Supporting Information shows several examples of missed  
529 detections that resulted from the STA/LTA inflexibility. Given its performance, STA/LTA is  
530 likely suitable for real-time seismic event detection applications, particularly in situations where  
531 an existing, trained model is not available. This method is applicable for systems such as  
532 earthquake early warning and volcanic monitoring, which require rapid results. It is important to  
533 note that in these scenarios, the immediate availability of results may be prioritized, even if it  
534 means accepting a higher likelihood of false positive detections for lower magnitude events (*e.g.*,  
535 Kumar et al., 2018; Li et al., 2016; Meier et al., 2020; Tepp, 2018).

536         The MF approach detects events with high precision, particularly if the events have a  
537 high degree of waveform similarity. However, developing a comprehensive set of template  
538 events can be time consuming, and the need to compare each of those templates to the  
539 continuous data can be computationally demanding (Liu et al., 2020; Meng et al., 2012). Further,  
540 since the MF technique is heavily dependent on the pre-defined templates, it is susceptible to  
541 missing events that diverge from recognized patterns (Gardonio et al., 2019; Kato & Nakagawa,  
542 2014; Peng & Zhao, 2009; Ross et al., 2018). Several examples of such missed events are shown  
543 in Figure S3 in the Supporting Information. Automatic event detection with this method is best-

544 suited to environments where the seismic events are self-similar, such as volcanic-related seismic  
545 swarms (*e.g.*, Tan et al., 2023; Whidden et al., 2023; Wimez & Frank, 2022) and repeating stick-  
546 slip activity beneath glaciers (*e.g.*, Helmstetter, 2022; Lucas et al., 2023; Ma et al., 2020).

547         Deep learning event detection techniques can help to address some of the problems faced  
548 by the STA/LTA and the MF approaches. Since deep learning models can be trained to recognize  
549 intricate seismic patterns, this approach has a greater degree of adaptability across a range of  
550 seismic signals and noise. Our analysis also illustrates how deep learning model performance can  
551 be further enhanced via transfer learning, where pre-trained models are adapted to recognize the  
552 characteristics of unique seismic sources (Chai et al., 2020; Liao et al., 2021). That said, deep  
553 learning approaches, with or without transfer learning, have their own set of challenges. ML  
554 methods are generally computationally intensive and do not provide rapid results (García et al.,  
555 2022; Zhu et al., 2022). Their performance is strongly linked to the quality and volume of their  
556 training subsets, and the oft-cited ‘black box’ nature of ML makes its decision-making processes  
557 ambiguous (Gonzalez Garibay et al., 2023). The effectiveness of transfer learning depends on  
558 whether the pre-trained model is relevant to the target dataset. If there is a mismatch between the  
559 source and target architecture, there is a risk of negative transfer, where the pre-trained model  
560 may fail to effectively adapt to the new task (Civilini et al., 2021; Zhou et al., 2021). Careful  
561 fine-tuning of the pre-trained model is needed to ensure its applicability to the specific seismic  
562 context, and this requires a certain level of understanding regarding the model’s architecture. All  
563 that said, seismic event catalogs based on ML models typically have a greater magnitude of  
564 completeness (*i.e.*, the minimum magnitude above which all events have been detected)  
565 compared to those generated by other approaches (Fig. 6; *e.g.*, Ma & Chen, 2022; Reynen &  
566 Audet, 2017; Ross et al., 2018). Therefore, if a given study requires robust, extensive seismic

567 constraints, the additional computational resources and complexity of ML algorithms are worth  
 568 the investment.



569

570 **Figure 6.** Histogram summarizing the number of events in each catalog after transfer learning  
 571 was applied, along with their corresponding local magnitude estimates. Light grey bars represent  
 572 the SL catalog, medium grey bars denote the ML catalog, and dark grey bars correspond to the  
 573 MF catalog.

574

## 575 *6.2 Preferred ML model for East Antarctica*

576

The metrics discussed in Sections 4.3 and 5 provide important information regarding the  
 577 most applicable model for a given seismic study. For our East Antarctic investigation, we  
 578 prioritized thorough seismic event detection. While it is important to identify events accurately  
 579 and precisely, the limited seismic station coverage in our study region (Fig. 1) emphasizes the  
 580 need to develop an event catalog that is as complete as possible. As such, our ideal model is one  
 581 that strikes a balance between sensitivity and accuracy, and our extensive analyses indicate that  
 582 the fine-tuned GPD model is an optimal choice. While EQT displays somewhat better pick  
 583 accuracy, as indicated by its RMSE and MAE values, its ability to distinguish between positive  
 584 and negative classes (AUC score) lags behind GPD (Tables 1-3). The trained GPD model's high  
 585 AUC score emphasizes that this model robustly distinguishes true events from noise. That is,  
 586 events with low SNR, potentially overlooked by other models and methods, are identified by

587 GPD. Furthermore, the inherent variability of seismic data demands a model that performs  
 588 consistently, and the GPD model displays consistent performance across all three examined  
 589 catalogs, both before and after transfer learning is applied (Tables 1-3). This indicates that the  
 590 GPD model is highly adaptable, regardless of the data's origin.

591

## 592 **7. Application**

### 593 *7.1 GPD Results for Each Catalog*

594 We applied the fine-tuned (transfer-learned) GPD model to the full suite of East Antarctic  
 595 data (2012-2015; Fig. 1), running three versions of the GPD detection algorithm concurrently,  
 596 corresponding to our SL, MF, and ML catalogs. As noted in Section 5, each model generates  
 597 pick probabilities for the designated P- and S-wave arrivals (Fig. 5). Picks with probabilities  
 598 below a specified threshold (Table 4) are discarded. These thresholds are essential for reducing  
 599 the number of spurious picks, thereby enhancing the accuracy and reliability of the detected  
 600 seismic events, and the thresholds ultimately control the number of event identifications. Table 4  
 601 summarizes the corresponding pick probability thresholds used to determine qualifying P- and S-  
 602 waves. These thresholds have led to the identification of new seismic events post-transfer  
 603 learning. Specifically, after transfer learning, the number of new events in the SL, ML, and MF  
 604 catalogs is 618, 372, and 201, respectively.

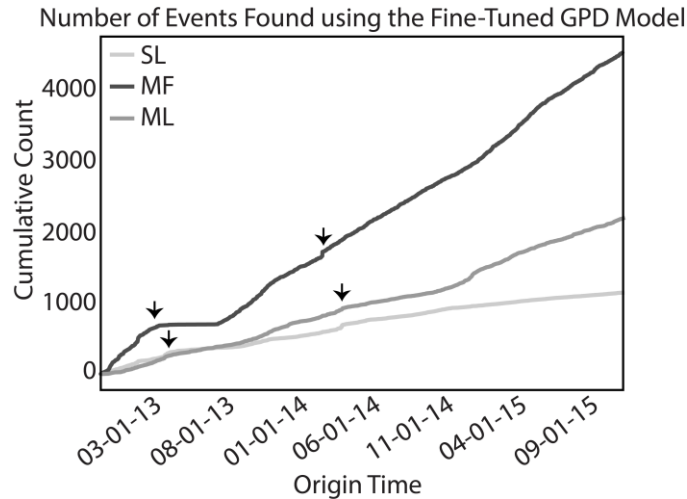
605

606 **Table 4.** P- and S-wave pick probability thresholds for the three transfer-learned catalogs. A P-  
 607 or S-wave pick is declared if the probability exceeds the specified threshold.

608

Catalog	P Threshold	S Threshold
ML	0.68	0.81
MF	0.42	0.51
SL	0.51	0.60

609



610

611 **Figure 7.** Cumulative number of events included in each catalog after transfer learning was  
 612 applied. The light grey line corresponds to the SL catalog, the dark grey line corresponds to the  
 613 MF catalog, and the medium grey line corresponds to the ML catalog. Arrows denote time  
 614 periods where an increased number of events are observed.

615

616 All three catalogs display an increase in the number of events around May 2013 and May

617 2014 (Fig. 7). These time periods correlate with seasonal changes in Antarctica as the austral

618 winter sets in. Tensile stresses in the ice sheet can be influenced by temperature, and this can

619 impact the formation of crevasses (Harper et al., 1998; Holdsworth, 1969). Specifically, when

620 temperatures drop, the surface layers of the ice sheet can become substantially colder than the

621 underlying firn, and this temperature gradient subjects the colder, more brittle surface layers to

622 an increase in tensile stress. Consequently, new crevasses may form and propagate along the ice

623 sheet surface (Nath & Vaughan, 2003), thereby leading to an increased number of icequakes.

624 This may explain the increase in detected events at these particular time intervals (Fig. 7). Local

625 magnitudes ( $M_L$ ) were also computed for the SL, ML, and MF catalog events (Fig. 6), though we

626 note that the magnitudes were determined using amplitude attenuation parameters developed for

627 southern California (Hutton & Boore, 1987). While not specific to our study region, these

628 parameters do not impact our assessment since our goal was to simply determine relative event

629 magnitudes rather than to make any interpretations of absolute magnitude. As shown in Figure 6,  
630 all three techniques effectively detect low magnitude ( $M_L \leq 3$ ) seismic events, though the ML  
631 technique detects a higher number of signals with magnitudes below two.

632

## 633 *7.2 Event Relocations*

634 After the fine-tuned GPD model was applied to the full East Antarctic dataset, as  
635 described in Section 7.1, the events from each of the updated catalogs were relocated using the  
636 NonLinLoc software package (Lomax et al., 2000). An equal differential-time likelihood  
637 function and the Oct-Tree sampling approach were used to compute the maximum likelihood  
638 hypocenters, based on the corresponding probability density functions (PDFs; Lomax et al.,  
639 2000; Zhou, 1994). We also utilized a modified version of the crustal velocity model (Fig. S4 in  
640 Supporting Information) from Pyle et al. (2010), which was developed for a nearby region in  
641 East Antarctica. Only earthquakes with at least four P- and S-wave arrival times were relocated.  
642 Additionally, to account for any possible bias in the procedure, we performed a second inversion  
643 using the average arrival-time residuals at each station (Lomax et al., 2009), thereby leading to  
644 better constrained event locations.

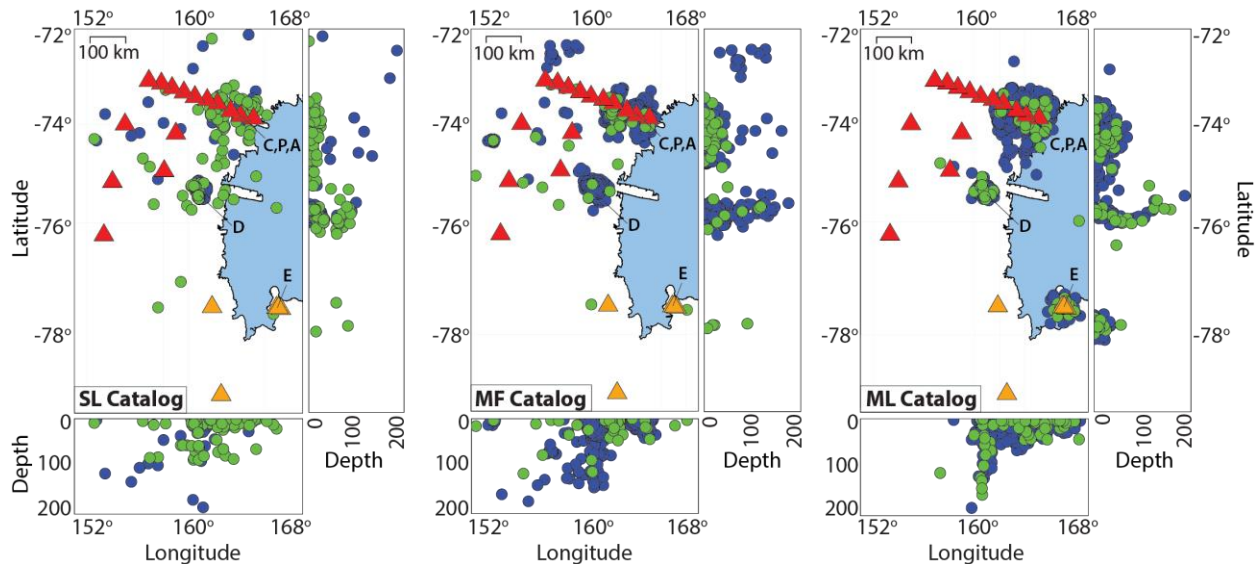
645 For each event relocation, the average horizontal and vertical uncertainties of the  
646 confidence ellipsoid, which are estimated by the PDFs, were used to determine the volume of the  
647 68% confidence ellipse. This, in turn, was used to determine the average uncertainty ( $R_e$ ) of each  
648 event location (Lomax et al., 2000). The relocated events in each catalog were then grouped  
649 based on their uncertainty thresholds. The best constrained event locations (Group A) had  $R_e \leq 5$   
650 km. Groups B, C, and D had progressively higher  $R_e$  values (Group B:  $5 < R_e \leq 10$  km; Group C:  
651  $10 < R_e \leq 20$  km; Group D:  $R_e \geq 20$  km), indicating less well-constrained locations. The number

652 of events in each quality group is provided in Table S1 in the Supporting Information. Figure 8  
653 highlights event locations that had  $R_e \leq 10$  km (*i.e.*, Groups A and B) within each catalog, and  
654 events from all groups are shown in Figure S5 in the Supporting Information.

655 Many of the detected events in all three catalogs are situated near David Glacier (Fig. 8).  
656 Shallow events ( $< 5$  km) in this region are consistent with those identified in previous studies  
657 (*e.g.*, Bannister & Kennett, 2002; Danesi et al., 2007, 2022; Zoet et al., 2012; 2013), which have  
658 been attributed to stick-slip behavior at the base of the ice sheet. However, all three catalogs also  
659 show deeper events ( $> 10$  km) beneath the David Glacier region as well, which could be  
660 associated with solid Earth processes. For example, movement and mass redistribution within the  
661 East Antarctic ice sheet may induce stress changes in the underlying lithosphere, creating the  
662 deep-seated events highlighted in our catalogs (Lund, 2015; Steffen, 2013; Steffen et al., 2020).

663 All three event catalogs also show notable seismicity beneath Victoria Land, in the  
664 northeastern portion of the study region (Fig. 8). The prevalence of event detections in this area  
665 may reflect some degree of spatial bias given the locations of the stations available for this study  
666 (Fig. 1). The TAMNNET stations, in particular, provide somewhat better coverage in this region;  
667 therefore, nearby events may more likely meet the enforced minimum number of P- and S-wave  
668 arrivals needed for relocation. That said, the Victoria Land event cluster (Fig. 8) is concentrated  
669 near several other glaciers that move across the Transantarctic Mountains and towards the Ross  
670 Sea, including the Campbell, Priestley, and Aviator Glaciers. The best located events in this  
671 cluster are relatively shallow and therefore may reflect ice-bed processes, similar to those  
672 suggested for David Glacier further to the south. Deeper events are also seen beneath this region,  
673 down to about 25-50 km, which are more likely associated with tectonic processes, such as  
674 faulting (*e.g.*, Pisarska-Jamrozy et al., 2018), or with crustal deformation driven by cryospheric

675 fluctuations (*e.g.*, Stewart et al., 2000). Further investigations would be needed to evaluate the  
 676 sources of the seismic events beneath David Glacier and Victoria Land, but the automatically  
 677 identified events from our analyses provide some insight into the complex relationship between  
 678 the solid Earth structure and the Antarctic ice sheet.



679 **Figure 8.** Seismic event relocations from NonLinLoc for quality Group A and B events. From  
 680 left to right: SL catalog, MF catalog, and ML catalog. Blue circles denote events that were  
 681 detected by the corresponding original technique (*i.e.*, STA/LTA, template matching, EQT  
 682 machine learning). Green circles denote new events detected by transfer learning. Red triangles  
 683 indicate TAMMNET stations, and orange triangles denote other stations. Abbreviations denote  
 684 key locations including David Glacier (D), Campbell, Priestly, and Aviator Glaciers (C,P,A), and  
 685 Mount Erebus (E).  
 686

687  
 688 It is also worth noting the cluster of seismic events near Mount Erebus, which was  
 689 uniquely identified by the ML catalog (Fig. 8). Some prior studies that have also recognized  
 690 seismicity in this region attribute the events to small magnitude icequake sources near the  
 691 volcano's summit (Chaput et al., 2015; Li et al., 2021; Podolskiy & Walter, 2016). Other  
 692 investigations have attributed the Mount Erebus seismicity to volcanic activity within its shallow  
 693 magmatic system (*e.g.*, Aster et al., 2008; Hansen & Schmandt, 2015; Kaminuma, 1987; Rowe et  
 694 al., 1998, 2000). The absence of the Mount Erebus event cluster in the SL and MF catalogs

695 underscores the effectiveness of deep learning techniques in seismic detection, particularly in  
696 elucidating events with a range of sources.

## 697 **8. Conclusions**

698 Our study has evaluated the benefits and limitations of different automated seismic event  
699 detection methods, and our results emphasize that the most appropriate approach depends on the  
700 specific attributes of the examined data as well as the objectives of a given study. The STA/LTA  
701 method is well-suited for real-time event detection applications that require rapid results, even if  
702 there is a higher likelihood for false detections. The MF technique works well for environments  
703 that generate seismic events with a high degree of waveform similarity. Deep learning models  
704 offer the most adaptability if dealing with a range of seismic sources and noise, and their  
705 performance can be enhanced with transfer learning, which provides an effective approach to  
706 adapt pre-trained models for unique datasets.

707 For our East Antarctic investigation, the fine-tuned GPD model, characterized by its high  
708 AUC score, reliable picking accuracy, and consistent performance across the examined catalogs,  
709 emerged as the most robust, providing new insights into seismic sources in the region. Event  
710 relocations based on the fine-tuned catalogs offer new insights into potential seismic sources,  
711 including both shallow cryospheric and deeper tectonic processes. Arguably, the most  
712 comprehensive seismic event catalog would be one created by integrating the results from each  
713 of the applied detection methods; however, the separate results highlight the performance of each  
714 approach. Our findings have expanded seismic event detections in East Antarctica, including the  
715 identification of previously unrecognized seismicity, and these results underscore the potential  
716 for automated event detection approaches to enhance our understanding of seismic activity even  
717 in areas with limited station coverage.

718

719

720 **Acknowledgments**

721 Funding for this research was provided by the National Science Foundation (grants OPP-  
722 1914698 (SEH), EAR-1745135 (JIW), and EAR-1925965 (ZP)), the Ministerio de Ciencia e  
723 Innovación / Agencia Estatal de Investigación (MCIN/AEI/10.13039/501100011033), and the  
724 European Union Next Generation EU “Plan de Recuperación, Transformación y Resiliencia”  
725 (PRTR; grant Model\_SHaKER, PID2021-124155NB-C31 (JLSR)).

726  
727 **Open Research**

728 The facilities of SAGE Data Services, particularly the SAGE Data Management Center,  
729 were used to access the waveforms and related metadata used in this project  
730 (<http://ds.iris.edu/mda/>). Specifically, we employed datasets from ASL/USGS (1993) and  
731 Hansen (2012). SAGE Data Services are funded through the Seismological Facilities for the  
732 Advancement of Geoscience (SAGE) Award of the National Science Foundation under  
733 Cooperative Support Agreement EAR-1851048. Some figures were generated with the Generic  
734 Mapping Tools software (Wessel et al., 2013). Our ML catalog was developed with the  
735 easyQuake software package (Walter et al., 2021; Walter, 2022), and transfer learning was  
736 implemented with Seisbench (Ho, 2024; Woollam et al., 2022).

737

738

739 **References**

- 740 Albuquerque Seismological Laboratory (ASL)/USGS (1993). Global Telemetered Seismograph  
741 Network [Dataset]. International Federation of Digital Seismograph Networks, doi:  
742 10.7914/SN/GT.
- 743 Allen, R. (1978). Automatic earthquake recognition and timing from single traces. *Bulletin of the*  
744 *Seismological Society of America*, 68(5), 1521–1532, doi: 10.1785/BSSA0680051521
- 745 Anandakrishnan, S., Voigt, D. E., Burkett, P. G., Long, B., & Henry, R. (2000). Deployment of a  
746 broadband seismic network in West Antarctica. *Geophysical Research Letters*, 27(14),  
747 2053-2056, doi: 10.1029/1999GL011189
- 748 Anthony, R. E., Aster, R. C., Wiens, D., Nyblade, A., Anandakrishnan, S., Huerta, A., Winberry,  
749 J. P., Wilson, T. & Rowe, C. (2015). The seismic noise environment of Antarctica.  
750 *Seismological Research Letters*, 86(1), 89-100, doi: 10.1785/0220140109
- 751 Aster, R., Zandomenighi, D., Mah, S., McNamara, S., Henderson, D. B., Knox, H., & Jones, K.  
752 (2008). Moment tensor inversion of very long period seismic signals from Strombolian  
753 eruptions of Erebus Volcano. *Journal of Volcanology and Geothermal Research*, 177(3),  
754 635-647, doi: 10.1016/j.jvolgeores.2008.08.013
- 755 Baer, M., & Kradolfer, U. (1987). An automatic phase picker for local and teleseismic events.  
756 *Bulletin of the Seismological Society of America*, 77(4), 1437–1445, doi:  
757 10.1785/BSSA0770041437
- 758 Bannister, S., & Kennett, B. L. N. (2002). Seismic Activity in the Transantarctic Mountains -  
759 Results from a Broadband Array Deployment. *Terra Antarctica*, 9, 41-46.

- 760 Bentley, C. R., & Kohnen, H. (1976). Seismic refraction measurements of internal friction in  
761 Antarctic ice. *Journal of Geophysical Research: Solid Earth*, 81(8), 1519-1526, doi:  
762 10.1029/JB081i008p01519
- 763 Boulder Real Time Technologies (BRTT; 2011). Evolution of the Commercial ANTELOPE  
764 Software.
- 765 Chai, C., Maceira, M., Santos-Villalobos, H. J., Venkatakrishnan, S. V., Schoenball, M., Zhu,  
766 W., Beroza, G. C., Thurber, C., & EGS Collaboration Team (2020). Using a deep neural  
767 network and transfer learning to bridge scales for seismic phase picking. *Geophysical*  
768 *Research Letters*, 47(16), doi: 10.1029/2020GL088651
- 769 Chamberlain, C. J., Hopp, C. J., Boese, C. M., Warren-Smith, E., Chambers, D., Chu, S. X.,  
770 Michailos, K., & Townend, J. (2018). EQcorrscan: Repeating and near-repeating  
771 earthquake detection and analysis in Python. *Seismological Research Letters*, 89(1), 173-  
772 181, doi: 10.1785/0220170151
- 773 Chaput, J., Campillo, M., Aster, R. C., Roux, P., Kyle, P. R., Knox, H., & Czoski, P. (2015).  
774 Multiple scattering from icequakes at Erebus volcano, Antarctica: Implications for  
775 imaging at glaciated volcanoes. *Journal of Geophysical Research: Solid Earth*, 120(2),  
776 1129-1141, doi: 10.1002/2014JB011278
- 777 Chen, X., Shearer, P. M., Walter, F., & Fricker, H. A. (2011). Seventeen Antarctic seismic  
778 events detected by global surface waves and a possible link to calving events from  
779 satellite images. *Journal of Geophysical Research: Solid Earth*, 116(B6), doi:  
780 10.1029/2011JB008262

- 781 Chen, C., and A. A. Holland (2016). PhasePApy: A Robust Pure Python Package for Automatic  
782 Identification of Seismic Phases, *Seismological Research Letters*, 87(6), doi:  
783 10.1785/0220160019
- 784 Chicco, D., & Jurman, G. (2020). The advantages of the Matthews correlation coefficient (MCC)  
785 over F1 score and accuracy in binary classification evaluation. *BMC Genomics*, 21(1),  
786 doi: 10.1186/s12864-019-6413-7
- 787 Cianetti, S., Bruni, R., Gaviano, S., Keir, D., Piccinini, D., Saccorotti, G., & Giunchi, C. (2021).  
788 Comparison of deep learning techniques for the investigation of a seismic sequence: An  
789 application to the 2019, Mw 4.5 Mugello (Italy) earthquake. *Journal of Geophysical*  
790 *Research: Solid Earth*, 126(12), doi: 10.1029/2021JB023405
- 791 Civilini, F., Weber, R. C., Jiang, Z., Phillips, D., & Pan, W. D. (2021). Detecting moonquakes  
792 using convolutional neural networks, a non-local training set, and transfer learning.  
793 *Geophysical Journal International*, 225(3), 2120-2134, doi: 10.1093/gji/ggab083
- 794 Coleman, C., Narayanan, D., Kang, D., Zhao, T., Zhang, J., Nardi, L., et al. (2017). Dawnbench:  
795 An end-to-end deep learning benchmark and competition. *Training*, 100(101), 102.
- 796 Danesi, S., Bannister, S., & Morelli, A. (2007). Repeating earthquakes from rupture of an  
797 asperity under an Antarctic outlet glacier. *Earth and Planetary Science Letters*, 253, 151-  
798 158, doi: 10.1016/j.epsl.2006.10.023
- 799 Danesi, S., Salimbeni, S., Borghi, A., Urbini, S., & Frezzotti, M. (2022). Cryo-seismicity  
800 triggered by ice mass discharge through the Antarctic subglacial hydrographic network.  
801 *The Cryosphere Discussions*, doi: 10.5194/egusphere-2022-29.

- 802 Earle, P. S., & Shearer, P. M. (1994). Characterization of global seismograms using an  
803 automatic-picking algorithm. *Bulletin of the Seismological Society of America*, 84(2),  
804 366-376, doi: 10.1785/BSSA0840020366
- 805 Fawcett, T. (2006). An introduction to ROC analysis. *Pattern Recognition Letters*, 27(8), 861-  
806 874, doi: 10.1016/j.patrec.2005.10.010
- 807 García, J. E., Fernández-Prieto, L. M., Villaseñor, A., Sanz, V., Ammirati, J. B., Díaz Suárez, E.  
808 A., & García, C. (2022). Performance of deep learning pickers in routine network  
809 processing applications. *Seismological Society of America*, 93(5), 2529-2542, doi:  
810 10.1785/0220210323
- 811 Gardonio, B., Campillo, M., Marsan, D., Lecointre, A., Bouchon, M., & Letort, J. (2019).  
812 Seismic activity preceding the 2011 M w 9.0 Tohoku earthquake, Japan, analyzed with  
813 multidimensional template matching. *Journal of Geophysical Research: Solid Earth*,  
814 124(7), 6815-6831, doi: 10.1029/2018JB016751
- 815 Gers, F. A., Schmidhuber, J., & Cummins, F. (1999). Learning to forget: continual prediction  
816 with LSTM, *Ninth International Conference on Artificial Neural Networks ICANN 99*.  
817 (*Conf. Publ. No. 470*), Edinburgh, UK, 850-855, doi: 10.1049/cp:19991218.
- 818 Gibbons, S. J., & Ringdal, F. (2006). The detection of low magnitude seismic events using array-  
819 based waveform correlation, *Geophysical Journal International*, 165(1), 149–166, doi:  
820 10.1111/j.1365-246X.2006.02865.x
- 821 González Garibay, M., Primc, K., & Slabe-Erker, R. (2023). Insights into advanced models for  
822 energy poverty forecasting. *Nature Energy*, 8, 903-905, doi: 10.1038/s41560-023-01311-  
823 x

- 824 Goodfellow, I., Bengio, Y., & Courville, A. (2016). *Deep Learning*. MIT Press, ISBN:  
825 9780262035613.
- 826 Guerin, G., Mordret, A., Rivet, D., Lipovsky, B. P., & Minchew, B. M. (2021). Frictional origin  
827 of slip events of the Whillans Ice Stream, Antarctica. *Geophysical Research Letters*,  
828 48(11), doi: 10.1029/2021GL092950.
- 829 Hampel, F. (1974). The influence curve and its role in robust estimation. *Journal of the*  
830 *American Statistical Association*, 69, 383-393, doi: 10.1080/01621459.1974.10482962
- 831 Han, J., Kim, S., Sheen, D. H., Lee, D., Lee, S. J., Yoo, S. H., & Park, D. (2023). Seismic event  
832 and phase detection using deep learning for the 2016 Gyeongju earthquake sequence.  
833 *Geosciences Journal*, 27(3), 285-295, doi: 10.1007/s12303-023-0004-y
- 834 Hanley, J. A. & McNeil, B. J. (1982). The meaning and use of the area under a receiver  
835 operating characteristic (ROC) curve. *Radiology*, 143(1), 29-36, doi:  
836 10.1148/radiology.143.1.7063747
- 837 Hansen, S. (2012). Transantarctic Mountains Northern Network [Dataset]. International  
838 Federation of Digital Seismograph Networks, doi: 10.7914/SN/ZJ\_2012.
- 839 Hansen, S. E., Reusch, A., Parker, T., Bloomquist, D., Carpenter, P., Graw, J. H., & Brenn, G. R.  
840 (2015). The Transantarctic Mountains Northern Network (TAMNNET): Deployment and  
841 Performance of a Seismic Array in Antarctica. *Seismological Research Letters*, 86, 1636-  
842 1644, doi: 10.1785/0220150117
- 843 Hansen, S. M., & Schmandt, B. (2015). Automated detection and location of microseismicity at  
844 Mount St. Helens with a large-N geophone array. *Geophysical Research Letters*, 42(18),  
845 7390-7397, doi: 10.1002/2015GL064848

- 846 Harper, J. T., Humphrey, N.F., & Pfeffer, W. T. (1998). Crevasse patterns and the strain-rate  
847 tensor: A high resolution comparison, *Journal of Glaciology*, *44*, 68-77, doi:  
848 10.3189/S0022143000002367
- 849 Heeszel, D. S., Wiens, D. A., Nyblade, A. A., Hansen, S. E., Kanao, M., An, M., & Zhao, Y.  
850 (2013). Rayleigh wave constraints on the structure and tectonic history of the  
851 Gamburtsev Subglacial Mountains, East Antarctica. *Journal of Geophysical Research:*  
852 *Solid Earth*, *118*(5), 2138-2153, doi: <https://doi.org/10.1002/jgrb.50171>
- 853 Helmstetter, A. (2022). Repeating Low Frequency Icequakes in the Mont-Blanc Massif  
854 Triggered by Snowfalls. *Journal of Geophysical Research: Earth Surface*, *127*(12), doi:  
855 10.1029/2022JF006837
- 856 Herrmann, M., & Marzocchi, W. (2021). Inconsistencies and lurking pitfalls in the magnitude–  
857 frequency distribution of high-resolution earthquake catalogs. *Seismological Research*  
858 *Letters*, *92*(2A), 909-922, doi: 10.1785/0220200337
- 859 Ho, L. M. (2024). Transfer\_Learning\_and\_Seisbench [Software], GitHub,  
860 [https://github.com/longmho/Transfer\\_Learning\\_and\\_Seisbench](https://github.com/longmho/Transfer_Learning_and_Seisbench).
- 861 Holdsworth, G. (1969). Primary transverse crevasses, *Journal of Glaciology*, *8*, 107-129.
- 862 Hudson, T. S., Kufner, S. K., Brisbourne, A. M., Kendall, J. M., Smith, A. M., Alley, R. B., et al.  
863 (2023). Highly variable friction and slip observed at Antarctic ice stream bed. *Nature*  
864 *Geoscience*, *16*, 612-618, doi: 10.1038/s41561-023-01204-4
- 865 Hutton, L. K., & Boore, D. M. (1987). The ML scale in south California, *Bulletin of the*  
866 *Seismological Society of America*, *77*(6), 2074-2094, doi: 10.1785/BSSA0740051827

- 867 Jiang, C., Fang, L., Fan, L., & Li, B. (2021). Comparison of the earthquake detection abilities of  
868 PhaseNet and EQTransformer with the Yangbi and Maduo earthquakes. *Earthquake*  
869 *Science*, 34(5), 425-435, doi: 10.29382/eqs-2021-0038
- 870 Kaminuma, K. (1987). Seismic activity of Erebus volcano, Antarctica. *Pure and Applied*  
871 *Geophysics*, 125, 993-1008, doi: 10.1007/BF00879364
- 872 Kato, A., Obara, K., Igarashi, T., Tsuruoka, H., Nakagawa, S., & Hirata, N. (2012). Propagation  
873 of slow slip leading up to the 2011 M w 9.0 Tohoku-Oki earthquake. *Science*, 335(6069),  
874 705-708, doi: 10.1126/science.1215141
- 875 Kato, A., & Nakagawa, S. (2014). Multiple slow-slip events during a foreshock sequence of the  
876 2014 Iquique, Chile Mw 8.1 earthquake. *Geophysical Research Letters*, 41(15), 5420-  
877 5427, doi: 10.1002/2014GL061138
- 878 Kennett, B. L. N., & Engdahl, E. R. (1991). Traveltimes for global earthquake location and phase  
879 identification. *Geophysical Journal International*, 105(2), 429-465, doi: 10.1111/j.1365-  
880 246X.1991.tb06724.x
- 881 Kingma, D. P., & Ba, J. (2014). Adam: A method for stochastic optimization. *arXiv preprint*  
882 *arXiv:1412.6980*.
- 883 Kumar, S., Vig, R., & Kapur, P. (2018). Development of Earthquake Event Detection Technique  
884 Based on STA/LTA Algorithm for Seismic Alert System. *Journal of the Geological*  
885 *Society of India*, 92, 679-686, doi: 10.1007/s12594-018-1087-3
- 886 Lapins, S., Goitom, B., Kendall, J. M., Werner, M. J., Cashman, K. V., & Hammond, J. O.  
887 (2021). A little data goes a long way: Automating seismic phase arrival picking at Nabro  
888 volcano with transfer learning. *Journal of Geophysical Research: Solid Earth*,  
889 126(7), doi: 10.1029/2021JB021910.

- 890 Li, X., Shang, X., Wang, Z., Dong, L., & Weng, L. (2016). Identifying P-phase arrivals with  
891 noise: An improved Kurtosis method based on DWT and STA/LTA. *Journal of Applied*  
892 *Geophysics*, 133, 50-61, doi: 10.1016/j.jappgeo.2016.07.022
- 893 Li, Z., Peng, Z., Hollis, D., Zhu, L., & McClellan, J. (2018). High-resolution seismic event  
894 detection using local similarity for Large-N arrays. *Scientific Reports*, 8(1), doi:  
895 10.1038/s41598-018-19728-w.
- 896 Li, C., Peng, Z., Chaput, J. A., Walter, J. I., & Aster, R. C. (2021). Remote triggering of  
897 Icequakes at Mt. Erebus, Antarctica by large teleseismic earthquakes. *Seismological*  
898 *Research Letters*, 92(5), 2866-2875, doi: 10.1785/0220210027
- 899 Liao, W., Chen, X., Lu, X., Huang, Y., & Tian, Y. (2021). Deep transfer learning and time-  
900 frequency characteristics-based identification method for structural seismic response.  
901 *Frontiers in Built Environment*, 7, doi: 10.3389/fbuil.2021.627058.
- 902 Liu, M., Li, H., Zhang, M., & Wang, T. (2020). Graphics processing unit-based match and locate  
903 (GPU-M&L): An improved match and locate method and its application. *Seismological*  
904 *Research Letters*, 91(2A), 1019-1029, doi: 10.1785/0220190241
- 905 Lomax, A., Virieux, J., Volant, P., & Berge-Thierry, C. (2000). Probabilistic earthquake location  
906 in 3D and layered models. In *Advances in Seismic Event Location*, eds. C.H. Thurber &  
907 N. Rabinowitz, 101-134, doi: 10.1007/978094-015-9536-0\_5.
- 908 Lomax, A., Michelini, A., Curtis, A., & Meyers, R. A. (2009). Earthquake location, direct,  
909 global-search methods. *Encyclopedia of Complexity and Systems Science*, 5, 2449-2473,  
910 doi:10.1007/978-0-387-30440-3

- 911 Long, M., Wang, J., Ding, G., Sun, J., & Yu, P. S. (2013). Transfer Feature Learning with Joint  
912 Distribution Adaptation. *Proceedings of the IEEE International Conference on Computer  
913 Vision*, 2200–2207.
- 914 Long, M., Cao, Z., Wang, J., & Jordan, M. I. (2015). Learning transferable features with deep  
915 adaptation networks. *Proceedings of the 32nd International conference on machine  
916 learning*, 97-105.
- 917 Lough, A. C., Wiens, D. A., Barcheck, G.C., Anandakrishnan, S., Aster, R. C., Blankenship, D.  
918 D., et al. (2013). Seismic detection of an active subglacial magmatic complex in Marie  
919 Byrd Land, Antarctica. *Nature Geoscience*, 6(12), 1031-1035, doi: 10.1038/ngeo1992
- 920 Lough, A. C., Wiens, D. A., & Nyblade, A. (2018). Reactivation of ancient Antarctic rift zones  
921 by intraplate seismicity. *Nature Geoscience*, 11(7), 515-519, doi: 10.1038/s41561-018-  
922 0140-6
- 923 Lucas, E. M., Nyblade, A. A., Aster, R. C., Wiens, D. A., Wilson, T. J., Winberry, J. P., &  
924 Huerta, A. D. (2023). Tidally Modulated Glacial Seismicity at the Foundation Ice Stream,  
925 West Antarctica. *Journal of Geophysical Research: Earth Surface*, 128(7), doi:  
926 10.1029/2023JF007172.
- 927 Lund, B. (2015). Palaeoseismology of Glaciated Terrain. *Encyclopedia of Earthquake  
928 Engineering*, Springer, Berlin, doi: 10.1007/978-3-642-36197-5\_25-1.
- 929 Ma, H., Chu, R., Sheng, M., & Yu, Z. (2020). Template matching for simple waveforms with  
930 low signal-to-noise ratio and its application to icequake detection. *Earthquake Science*,  
931 33, 256-263, doi: 10.29382/eqs-2020-0256-01

- 932 Ma, X., & Chen, T. (2022). Small Seismic Events in Oklahoma Detected and Located by  
933 Machine Learning–Based Models. *Bulletin of the Seismological Society of America*,  
934 *112*(6), 2859-2869.
- 935 Matthews, B. W. (1975). Comparison of the predicted and observed secondary structure of T4  
936 phage lysozyme. *Biochimica et Biophysica Acta (BBA)-Protein Structure*, *405*(2), 442-  
937 451, doi: 10.1016/0005-2795(75)90109-9
- 938 Meier, M. A., Kodera, Y., Böse, M., Chung, A., Hoshihara, M., Cochran, E., et al. (2020). How  
939 often can earthquake early warning systems alert sites with high-intensity ground  
940 motion?. *Journal of Geophysical Research: Solid Earth*, *125*(2), doi:  
941 10.1029/2019JB017718
- 942 Meng, X., Yu, X., Peng, Z., & Hong, B. (2012). Detecting earthquakes around Salton Sea  
943 following the 2010 Mw7. 2 El Mayor-Cucapah earthquake using GPU parallel  
944 computing. *Procedia Computer Science*, *9*, 937-946, doi: 10.1016/j.procs.2012.04.100
- 945 Meng, X., Peng, Z., & Hardebeck, J. (2013). Seismicity around Parkfield correlates with static  
946 shear stress changes following the 2003 Mw6.5 San Simeon earthquake, *Journal of*  
947 *Geophysical Research*, *118*(7), 3576-3591, doi:10.1002/jgrb.50271
- 948 Mousavi, S. M., Sheng, Y., Zhu, W., & Beroza, G. C. (2019). STanford EArthquake Dataset  
949 (STEAD): A global data set of seismic signals for AI. *IEEE Access*, *7*, 179,464-179,476,  
950 doi: 10.1109/ACCESS.2019.2947848
- 951 Mousavi, S. M., Ellsworth, W. L., Zhu, W., Chuang, L. Y., & Beroza, G. C. (2020). Earthquake  
952 transformer—an attentive deep-learning model for simultaneous earthquake detection and  
953 phase picking. *Nature Communications*, *11*(1), doi: 10.1038/s41467-020-17591-w

- 954 Münchmeyer, J., Woollam, J., Rietbrock, A., Tilmann, F., Lange, D., Bornstein, T., et al. (2022).  
955 Which picker fits my data? A quantitative evaluation of deep learning based seismic  
956 pickers. *Journal of Geophysical Research: Solid Earth*, 127(1), doi:  
957 10.1029/2021JB023499
- 958 Myers, S. C., Johannesson, G., & Hanley, W. (2007). A Bayesian hierarchical method for  
959 multiple-event seismic location. *Geophysical Journal International*, 171(3), 1049–1063,  
960 doi: 0.1111/j.1365-246X.2007.03555.x
- 961 Nath, P. C., & Vaughan, D. G. (2003). Subsurface crevasse formation in glaciers and ice sheets.  
962 *Journal of Geophysical Research: Solid Earth*, 108(B1), doi: 10.1029/2001JB000453
- 963 Nettles, M., & Ekström, G. (2010). Glacial earthquakes in Greenland and Antarctica. *Annual*  
964 *Review of Earth and Planetary Sciences*, 38, 467-491, doi: 10.1146/annurev-earth-  
965 040809-152414
- 966 Neves, M., Chuang, L.Y., Li, W., Peng, Z., Figueiredo, P. M., & Ni, S. (2024). A dense  
967 microearthquake catalog reveals the complex rupture of the extremely shallow M5.1  
968 Sparta, North Carolina Earthquake. *Communications Earth & Environment*.
- 969 Pan, S. J. & Yang, Q. (2010). A survey on transfer learning. *IEEE Transactions on Knowledge*  
970 *and Data Engineering*, 22(10), 1345-1359, doi: 10.1109/TKDE.2009.191
- 971 Pan, S. J., Tsang, I. W., Kwok, J. T., & Yang, Q. (2011). Domain Adaptation via Transfer  
972 Component Analysis. *IEEE Transactions on Neural Networks*, 22(2), 199–210, doi:  
973 0.1109/TNN.2010.2091281
- 974 Peng, Z., & Zhao, P. (2009). Migration of early aftershocks following the 2004 Parkfield  
975 earthquake. *Nature Geoscience*, 2(12), 877-881, doi: 10.1038/ngeo697

- 976 Peng, Z., Walter, J. I., Aster, R. C., Nyblade, A., Wiens, D. A., & Anandakrishnan, S. (2014).  
977 Antarctic icequakes triggered by the 2010 Maule earthquake in Chile. *Nature*  
978 *Geoscience*, 7(9), 677-681, doi: 10.1038/ngeo2212
- 979 Perol, T., Gharbi, M., & Denolle, M. (2018). Convolutional neural network for earthquake  
980 detection and location. *Science Advances*, 4(2), doi: 10.1126/sciadv.170057
- 981 Pisarska-Jamrozý, M., Belzyt, S., Börner, A., Hoffmann, G., Hüneke, H., Kenzler, M., et al.  
982 (2018). Evidence from seismites for glacio-isostatically induced crustal faulting in front  
983 of an advancing land-ice mass (Rügen Island, SW Baltic Sea). *Tectonophysics*, 745, 338-  
984 348, doi: 10.1016/j.tecto.2018.08.004
- 985 Podolskiy, E. A., & Walter, F. (2016). Cryoseismology. *Reviews of Geophysics*, 54(4), 708-758.
- 986 Powers, D.M. (2011). Evaluation: from precision, recall and F-measure to ROC, informedness,  
987 markedness and correlation. *Journal of Machine Learning Technologies*, 2(1), 37-63, doi:  
988 10.48550/arXiv.2010.16061
- 989 Pyle, M. L., Wiens, D. A., Nyblade, A. A., & Anandakrishnan, S. (2010). Crustal structure of the  
990 Transantarctic Mountains near the Ross Sea from ambient seismic noise tomography.  
991 *Journal of Geophysical Research: Solid Earth*, 115(B11), doi: 10.1029/2009JB007081
- 992 Reynen, A., & Audet, P. (2017). Supervised machine learning on a network scale: application to  
993 seismic event classification and detection. *Geophysical Journal International*, 210(3),  
994 1394-1409, doi: 10.1093/gji/ggx238
- 995 Riel, B., Minchew, B., & Bischoff, T. (2021). Data-Driven Inference of the Mechanics of Slip  
996 Along Glacier Beds Using Physics-Informed Neural Networks: Case Study on Rutford  
997 Ice Stream, Antarctica. *Journal of Advances in Modeling Earth Systems*, 13(11), doi:  
998 10.1029/2021MS002621

- 999 Ronneberger, O., Fischer, P., & Brox, T. (2015). U-Net: Convolutional Networks for Biomedical  
1000 Image Segmentation. In *Medical Image Computing and Computer-Assisted Intervention*,  
1001 9351, 234-241, doi: 10.1007/978-3-319-24574-4\_28
- 1002 Ross, Z. E., Meier, M.-A., & Hauksson, E. (2018). P Wave Arrival Picking and First-Motion  
1003 Polarity Determination with Deep Learning. *Journal of Geophysical Research: Solid*  
1004 *Earth*, 123(6), 5120-5129, doi: 10.1029/2017JB015251
- 1005 Rowe, C. A., Aster, R. C., Kyle, P. R., Schlue, J. W., & Dibble, R. R. (1998). Broadband  
1006 recording of Strombolian explosions and associated very-long-period seismic signals on  
1007 Mount Erebus Volcano, Ross Island, Antarctica. *Geophysical Research Letters*, 25(13),  
1008 2297-2300, doi: 10.1029/98GL01622
- 1009 Rowe, C. A., Aster, R. C., Kyle, P. R., Dibble, R. R., & Schlue, J. W. (2000). Seismic and  
1010 acoustic observations at Mount Erebus volcano, Ross Island, Antarctica, 1994–1998.  
1011 *Journal of Volcanology and Geothermal Research*, 101(1-2), 105-128, doi:  
1012 10.1016/S0377-0273(00)00170-0
- 1013 Schaff, D. P., & Beroza, G. C. (2004). Coseismic and postseismic velocity changes measured by  
1014 repeating earthquakes. *Journal of Geophysical Research: Solid Earth*, 109(B10), doi:  
1015 10.1029/2004JB003011
- 1016 Shelly, D. R., Beroza, G. C., & Ide, S. (2007). Non-volcanic tremor and low-frequency  
1017 earthquake swarms. *Nature*, 446(7133), 305-307, doi: 10.1038/nature05666
- 1018 Si, X., Wu, X., Li, Z., Wang, S., & Zhu, J. (2024). An all-in-one seismic phase picking, location,  
1019 and association network for multi-task multi-station earthquake monitoring.  
1020 *Communications Earth & Environment*, 5(1), 22, doi: 10.1038/s43247-023-01188-4

- 1021 Skoumal, R. J., Brudzinski, M. R., & Currie, B. S. (2015). Earthquakes induced by hydraulic  
1022 fracturing in Poland Township, Ohio. *Bulletin of the Seismological Society of America*,  
1023 *105*(1), 189-197, doi: 10.1785/0120140168
- 1024 Smith, L. N. (2018). A disciplined approach to neural network hyper-parameters: Part 1--  
1025 learning rate, batch size, momentum, and weight decay. *US Naval Research Laboratory*  
1026 *Technical Report*, 5510-026, doi: 10.48550/arXiv.1803.09820
- 1027 Steffen, R. (2013). The influence of glacial isostatic adjustment on intraplate seismicity in  
1028 northeastern Canada. *Doctoral Thesis*, University of Calgary, Canada, doi:  
1029 10.11575/PRISM/28209
- 1030 Steffen, R., Steffen, H., Weiss, R., Lecavalier, B. S., Milne, G. A., Woodroffe, S. A., & Bennike,  
1031 O. (2020). Early Holocene Greenland-ice mass loss likely triggered earthquakes and  
1032 tsunamis. *Earth and Planetary Science Letters*, *546*, doi: 10.1016/j.epsl.2020.116443.
- 1033 Stewart, I. S., Sauber, J., & Rose, J. (2000). Glacio-seismotectonics: ice sheets, crustal  
1034 deformation and seismicity. *Quaternary Science Reviews*, *19*(14-15), 1367-1389, doi:  
1035 10.1016/S0277-3791(00)00094-9
- 1036 Tan, C., Sun, F., Kong, T., Zhang, W., Yang, C., & Liu, C. (2018). A survey on deep transfer  
1037 learning. In *Artificial Neural Networks and Machine Learning—ICANN 2018: 27th*  
1038 *International Conference on Artificial Neural Networks, Rhodes, Greece, October 4-7,*  
1039 *2018, Proceedings, Part III 27* (pp. 270-279). Springer International Publishing.
- 1040 Tan, D., Fee, D., Hotovec-Ellis, A. J., Pesicek, J.D., Haney, M.M., Power, J. A., & Girona, T.  
1041 (2023). Volcanic earthquake catalog enhancement using integrated detection, matched-  
1042 filtering, and relocation tools. *Frontiers in Earth Science*, *11*, doi:  
1043 10.3389/feart.2023.1158442

- 1044 Tepp, G. (2018). A Repeating Event Sequence Alarm for Monitoring Volcanoes. *Seismological*  
1045 *Research Letters*, 89(5), 1863-1876, doi: 10.1785/0220170263
- 1046 Trnkoczy, A. (2009). Understanding and parameter setting of STA/LTA trigger algorithm. In  
1047 *New manual of seismological observatory practice*, Deutsches GeoForschungsZentrum  
1048 GFZ, 1-20.
- 1049 Vaezi, Y., & Van der Baan, M. (2015). Comparison of the STA/LTA and power spectral density  
1050 methods for microseismic event detection. *Geophysical Supplements to the Monthly*  
1051 *Notices of the Royal Astronomical Society*, 203(3), 1896-1908, doi: 10.1093/gji/ggv419
- 1052 Waldhauser, F., & Schaff, D. (2007). Regional and teleseismic double-difference earthquake  
1053 relocation using waveform cross-correlation and global bulletin data. *Journal of*  
1054 *Geophysical Research: Solid Earth*, 112(B12), doi: 10.1029/2007JB004938
- 1055 Walter, J. I., E. E. Brodsky, S. Tulaczyk, S. Y. Schwartz, & R. Pettersson (2011). Transient slip  
1056 events from near-field seismic and geodetic data on a glacier fault, Whillans Ice Plain,  
1057 West Antarctica, *Journal of Geophysical Research: Solid Earth*, 116,  
1058 doi:10.1029/2010JF001754
- 1059 Walter, J. I., I. Svelitsky, J. Fineberg, S. Tulaczyk, E. E. Brodsky, C. G. Barcheck, & S. P.  
1060 Carter (2015). Rupture speed dependence on initial stress profiles: Insights from glacier  
1061 and laboratory stick-slip, *Earth and Planetary Science Letters*, 411, 112-120, doi:  
1062 10.1016/j.epsl.214.11.025
- 1063 Walter, J. I., Ogwari, P., Thiel, A., Ferrer, F., & Woelfel, I. (2021). easyQuake: Putting machine  
1064 learning to work for your regional seismic network or local earthquake study,  
1065 *Seismological Research Letters*, 92(1): 555–563, doi: 10.1785/0220200226
- 1066 Walter, J. I. (2022). easyQuake [Software], GitHub, <https://github.com/jakewalter/easyQuake>.

- 1067 Wessel, P., Smith, W. H., Scharroo, R., Luis, J., & Wobbe, F. (2013). Generic mapping tools:  
1068 improved version released. *Eos, Transactions American Geophysical Union*, 94(45), 409-  
1069 410, doi: 10.1002/2013EO450001
- 1070 Willmott, C. J., & Matsuura, K. (2005). Advantages of the mean absolute error (MAE) over the  
1071 root mean square error (RMSE) in assessing average model performance. *Climate*  
1072 *Research*, 30(1), 79-82, doi: 10.3354/cr030079
- 1073 Wimez, M., & Frank, W. B. (2022). A recursive matched-filter to systematically explore  
1074 volcanic long-period earthquake swarms. *Geophysical Journal International*, 231(2),  
1075 912-920, doi: 10.1093/gji/ggac221
- 1076 Winberry, J. P., Anandakrishnan, S., Alley, R. B., Wiens, D. A., & Pratt, M. J. (2014). Tidal  
1077 pacing, skipped slips and the slowdown of Whillans Ice Stream, Antarctica. *Journal of*  
1078 *Glaciology*, 60(222), 795-807, doi: 10.3189/2014JoG14J038
- 1079 Winberry, J. P., Huerta, A. D., Anandakrishnan, S., Aster, R.C., Nyblade, A.A., & Wiens, D. A.  
1080 (2020). Glacial earthquakes and precursory seismicity associated with Thwaites Glacier  
1081 calving. *Geophysical Research Letters*, 47(3), doi: 10.1029/2019GL086178
- 1082 Whidden, K. M., Petersen, G. M., Mesimeri, M., & Pankow, K. L. (2023). Analysis of the 2021  
1083 Milford, Utah earthquake swarm: Enhanced earthquake catalog and migration patterns.  
1084 *Frontiers in Earth Science*, 11, doi: 10.3389/feart.2023.1057982
- 1085 Woollam, J., Rietbrock, A., Bueno, A., & De Angelis, S. (2019). Convolutional neural network  
1086 for seismic phase classification, performance demonstration over a local seismic network.  
1087 *Seismological Research Letters*, 90(2A), 491– 502, doi: 10.1785/0220180312

- 1088 Woollam, J., Münchmeyer, J., Tilmann, F., Rietbrock, A., Lange, D., Bornstein, T., & Soto, H.  
1089 (2022). Seisbench-A toolbox for machine learning in seismology. *Seismological*  
1090 *Research Letters*, 81(3), 1695–1709, doi: 10.1785/0220210324
- 1091 Wu, Y., Lin, Y., Zhou, Z., Bolton, D. C., Liu, J., & Johnson, P. (2018). DeepDetect: A Cascaded  
1092 Region-Based Densely Connected Network for Seismic Event Detection, *IEEE*  
1093 *Transactions on Geoscience and Remote Sensing*, 57, 62-75, doi:  
1094 0.1109/TGRS.2018.2852302
- 1095 Yao, D., Peng, Z., Kaneko, Y., Fry, B., & Meng, X. (2021). Dynamic triggering of earthquakes  
1096 in the North Island of New Zealand following the 2016 Mw 7.8 Kaikōura earthquake.  
1097 *Earth and Planetary Science Letters*, 557, doi: 10.1016/j.epsl.2020.116723
- 1098 Yuan, C., Ni, Y., Lin, Y., & Denolle, M. (2023). Better Together: Ensemble Learning for  
1099 Earthquake Detection and Phase Picking. *IEEE Transactions on Geoscience and Remote*  
1100 *Sensing*, doi: 10.1109/TGRS.2023.3320148
- 1101 Yoon, C. E., O'Reilly, O., Bergen, K. J., & Beroza, G. C. (2015). Earthquake detection through  
1102 computationally efficient similarity search. *Science Advances*, 1(11), doi:  
1103 10.1126/sciadv.1501057
- 1104 Zhou, H. (1994). Rapid three-dimensional hypocentral determination using a master station  
1105 method. *Journal of Geophysical Research*, 99(B8), doi: 10.1029/94JB00934
- 1106 Zhou, Y., Yue, H., Kong, Q., & Zhou, S. (2019). Hybrid Event Detection and Phase-Picking  
1107 Algorithm Using Convolutional and Recurrent Neural Networks, *Seismological Research*  
1108 *Letters*, 90(3), 1079–1087, doi: 10.1785/0220180319
- 1109 Zhou, R., Yao, X., Hu, G., & Yu, F. (2021). Learning from unlabelled real seismic data: Fault  
1110 detection based on transfer learning. *Geophysical Prospecting*, 69(6), 1218-1234.

- 1111 Zhu, W. & Beroza, G. C. (2019). PhaseNet: A deep-neural-network-based seismic arrival-time  
1112 picking method. *Geophysical Research Letters*, 45(13), 6644-6653, doi:  
1113 10.1093/gji/ggy423
- 1114 Zhu, L., Peng, Z., McClellan, J., Li, C., Yao, D., Li, Z., & Fang, L. (2019). Deep learning for  
1115 seismic phase detection and picking in the aftershock zone of 2008 Mw 7.9 Wenchuan  
1116 Earthquake. *Physics of the Earth and Planetary Interiors*, 293, doi:  
1117 10.1016/j.pepi.2019.05.004
- 1118 Zhu, W., Tai, K. S., Mousavi, S. M., Bailis, P., & Beroza, G. C. (2022). An end-to-end  
1119 earthquake detection method for joint phase picking and association using deep learning.  
1120 *Journal of Geophysical Research: Solid Earth*, 127(3), doi: 10.1029/2021JB023283
- 1121 Zoet, L. K., Anandakrishnan, S., Alley, R. B., Nyblade, A. A., & Wiens, D. A. (2012). Motion of  
1122 an Antarctic glacier by repeated tidally modulated earthquakes. *Nature Geoscience*, 5(9),  
1123 623-626, doi: 10.1038/ngeo1555
- 1124 Zoet, L. K., Alley, R. B., Anandakrishnan, S., & Christianson, K. (2013). Accelerated subglacial  
1125 erosion in response to stick-slip motion. *Geology*, 41(2), 159-162 doi: 10.1130/G33624.1  
1126  
1127  
1128